INSTITUTE FOR DEFENSE ANALYSES

The Role of Defensive Postures in Computing Probability of Hit for Projectile Blunt Impact Intermediate Force Capabilities

Sujeeta B. Bhatt
Emily Cheng
Corinne M. Kramer
Jessica G. Swallow
Jeremy A. Teichman

January 2021

Approved for public release;
distribution is unlimited.

IDA Document D-21534

Log: H 21-000015

INSTITUTE FOR DEFENSE ANALYSES
4850 Mark Center Drive
Alexandria, Virginia 22311-1882

IDA

The Institute for Defense Analyses is a nonprofit corporation that operates three Federally Funded Research and Development Centers. Its mission is to answer the most challenging U.S. security and science policy questions with objective analysis, leveraging extraordinary scientific, technical, and analytic expertise.

About This Publication

This work was conducted by the IDA Systems and Analyses Center under contract HQ0034-14-D-0001, Project DU-2-4273, "IFC Modeling Uncertainty Analysis," for the Joint Intermediate Force Capabilities Office (JIFCO). The views, opinions, and findings should not be construed as representing the official position of either the Department of Defense or the sponsoring organization.

For More Information

Sujeeta B. Bhatt, Project Leader
sbhatt@ida.org, 703-578-2719

Leonard J. Buckley, Director, Science and Technology Division
lbuckley@ida.org, 703-578-2800

Copyright Notice

© 2021 Institute for Defense Analyses
4850 Mark Center Drive, Alexandria, Virginia 22311-1882 • (703) 845-2000.

This material may be reproduced by or for the U.S. Government pursuant to the copyright license under the clause at DFARS 252.227-7013 (Feb. 2014).

Rigorous Analysis | Trusted Expertise | Service to the Nation

INSTITUTE FOR DEFENSE ANALYSES

IDA Document D-21534

The Role of Defensive Postures in Computing Probability of Hit for Projectile Blunt Impact Intermediate Force Capabilities

Sujeeta B. Bhatt
Emily Cheng
Corinne M. Kramer
Jessica G. Swallow
Jeremy A. Teichman

Executive Summary

Background

Intermediate force capabilities (IFCs) are an essential tool that the military uses to control escalation of force in complex circumstances. A key step in the design and acquisition of IFCs is estimating risk of significant injury (RSI). RSI is defined as the probability that upon exposure to the weapon targets will develop an injury that will impair physiological function or restrict employment or other activities for the rest of his or her life (a permanent injury) if they do not receive professional medical care. The Joint Intermediate Force Capabilities Office (JIFCO) invests in developing models that can simulate blunt impacts and compute the risk of different types of injuries depending on the impact location. The aggregate risk of injury per impact from a blunt-impact weapon comprises the risk of injury for impacts to each body region weighted by the likelihood that each body region is hit, given that a hit to the target occurred. However, estimates of probability of hit (*p*(hit)) to individual body regions are typically based on the assumption that a target faces the weapon in a passive posture (standing, with arms to the sides). In reality, targets may engage in a range of defensive actions, such as ducking or crouching, turning to the side, or protecting the head or torso with their arms. In this report, we study the effect of such defensive postures on the *p*(hit) distribution for weapons with varying dispersion characteristics and aim points.

Approach

Using a Microsoft Kinect V2 sensor and the Image Acquisition Toolbox for Matlab, we collected depth and color images with concurrent computer tracking of skeleton joint positions for 26 volunteers in 13 specified defensive postures. The postures were designed to cover three key postural variables (orientation relative to the camera, upright/crouched, and arm position) in all possible combinations, as well as one example of the subject running away. Images were segmented into body regions and background with an automated segmentation algorithm. A virtual experiment was conducted by overlaying probabilistically generated weapon-impact locations (based on weapon dispersion characteristics) on segmented images. These data were used to compute the *p*(hit) for each body region and pose (for two aim points and 100 possible two-dimensional weapon-dispersion patterns) and generate a set of lookup tables. The effect of actions such as crouching, turning, protecting the head, protecting the arms, or running away on *p*(hit) distribution was then analyzed based on *p*(hit) distributions derived from pairs of poses differing only by these actions. The overall *p*(hit) for each body region for sets of notional posture distributions was explored to understand the aggregate effect of postural variation on estimates of *p*(hit). Finally, notional distributions of risk of injury given a hit to each body region were used to explore how differences in *p*(hit) distribution caused by defensive postures could affect RSI.

Results

Analysis of the synthetically generated dataset found that certain defensive actions have quantitative and systematic effects on *p*(hit) distributions for certain body regions. In particular, for a center torso aim point (common for blunt-impact weapons):

- Crouching reduces *p*(hit) to the abdomen and thorax while increasing *p*(hit) to the arms and legs and modestly increasing *p*(hit) to the head and pelvis.
- Turning to the side has complex interactions with *p*(hit) distribution, depending on the positions of the arms and whether the subject is also crouched.
- Protecting the head with the arms decreases *p*(hit) to the head and arms while increasing *p*(hit) to the abdomen, particularly at close range.
- Protecting the torso with the arms decreases *p*(hit) to the thorax while increasing *p*(hit) to the arms.
- Running away has a small effect on the *p*(hit) distribution at close range, but increases *p*(hit) to the abdomen and decreases *p*(hit) to the arms and head at long range.
- As weapon dispersion increases, *p*(hit) distributions spread out to cover more of the body, typically increasing *p*(hit) to the head, legs, and pelvis and decreasing *p*(hit) to the thorax and abdomen.

Many of these trends were consistent with results obtained for a belt-buckle aim point (another common aim point for blunt-impact weapons), except that *p*(hit) to the legs typically decreased with range while *p*(hit) to the thorax increased. Also, defensive-posture effects for the head, arms, and thorax were often smaller than observed for the center-torso aim point.

In the aggregate, crowds engaging in defensive postures will exhibit different *p*(hit) distributions than naïve crowds. We considered a number of notional distributions of postures and RSI for various body segments. Our analysis showed changes in overall RSI due to postural effects varying from only a few percentage points to as much as a factor of 2. Of the defensive actions analyzed, the combined action of crouching and protecting the torso with the arms had the largest effect on *p*(hit) distribution, transferring hits from the abdomen and thorax to the arms and legs. Depending on whether the limbs or trunk is more vulnerable to the weapon of interest, this could either increase or decrease RSI. These results indicate the importance of understanding the interaction of defensive postures, p(hit) distribution, and significant injury risks when conducting an RSI analysis. Our general analysis would need to be tailored to reflect the particular specifications of a given operational setting and weapon performance. Information about the probable effect of defensive postures on the risk of injury associated with use of particular weapons (especially risk *increases*) should be shared with the users of those weapons and should be considered when determining weapon concepts of operation (CONOPs). However, our results are encouraging in that they suggest that errors related to ignoring these factors in the past have probably been small relative to other uncertainties, such as determining injury risk given a hit to a particular location.

The analysis contained in this report has some important limitations. For example, the analysis does not consider more granular hit-position variability (e.g., impacts on- or off-rib in the torso). At the time of this writing, the sensitivity to impact location of JIFCO's existing blunt-impact injury models was under active exploration. Also, the automated segmentation methods used in the analysis could be improved to reduce bias for computing p(hit) for certain body regions or to further subdivide body regions (e.g., separate the upper and lower portions of the leg). More advanced segmentation methods and improved skeleton tracking in image collection, particularly for distinguishing the arms from the torso, would improve our estimates of posture effects on p(hit). Our data-collection approach could also have been improved by recruiting from a wider pool of potential subjects and including more realism in the image-collection process. We believe that our analysis methods can be adapted to new photographic or video-based data sources.

Although this report focused on RSI, our results and methods can also be applied to more detailed assessments of injury risk from blunt-impact weapons by helping identify what kinds of behaviors increase the chance of potentially fatal injuries vs. injuries that have a high chance of recovery with appropriate medical care.

This report concludes, based on quantitative analysis, that defensive postures can directly affect how impacts from a projectile fired from a blunt-impact weapon are distributed over the regions of the body. Because different regions of the body (e.g., arms, legs, head, thorax, abdomen, pelvis) can have different vulnerability to particular projectile types, changes in the distribution of impacts can affect the aggregate calculation of RSI for a particular weapon. Therefore, analysis of RSI should account for potential target responses to the IFC to inform the design, training, and CONOPs of each weapon.

Contents

1. Introduction

Intermediate force capabilities (IFCs)[1] are essential tools that the military uses to control escalation of force in complex circumstances. IFCs can be used to discriminate between hostile and non-hostile individuals, to stop or delay potentially hostile actions, or to incapacitate hostile individuals while minimizing risk to bystanders or collateral damage to surrounding infrastructure or equipment. IFCs are therefore critical to the success of the warfighter, especially in urban environments, where hostile actors, noncombatants, and critical infrastructure are likely to be close to each other and circumstances can change rapidly.

IFCs are "developed and used with the intent to minimize the probability of producing fatalities, significant or permanent injuries, or undesired damage to materiel, but do not, and are not intended to, eliminate risk of those actions entirely" (DoD 2013). A key step in the design and acquisition of IFCs is estimating risk of significant injury (RSI). RSI is defined as the probability that targets will develop an injury that will impair physiological function or restrict employment or other activities for the rest of their life (a permanent injury) or cause death if they do not receive at least health-care capability index 1 care. This health-care threshold (index 1 care) includes any care beyond self-aid or buddy aid (i.e., aid by a nonmedical professional).

The Joint Intermediate Force Capabilities Office (JIFCO) is responsible for managing the Department of Defense's Joint Non-Lethal Weapons Program, including funding research and development of IFC technology and human-effects modeling capabilities and supporting testing and evaluation of IFCs. This includes funding computational model development for estimating the RSI of various types of IFC.

RSI is a key informative parameter that helps designers ensure that their systems meet requirements, acquisitions professionals decide whether to acquire a particular IFC, and commanders decide when to employ an IFC. RSI is typically determined following Equation 1:

$$RSI = P(\text{injury occurred}) * P(\text{injury is significant}|\text{injury occurred}) \qquad (1)$$

We note that RSI does not include shots that fail to hit the target; RSI is the probability of significant injury given a single hit.

[1] Non-lethal weapons are a subset of IFCs.

Projectile blunt-impact IFCs, such as beanbag rounds, foam-nose projectiles, and rubber bullets, are one of the most common types of IFC. Although not intended to do so, blunt impact IFCs have the potential to produce a range of significant injuries such as fractured bones, internal organ lacerations, and lung contusions (Suyama et al. 2003; Rezende-Neto et al. 2009; Mahajna et al. 2002). To quantify RSI for blunt-impact weapons, JIFCO has invested in development of the Advanced Total Body Model (ATBM), which is a set of finite-element models that can be used to simulate blunt impacts and compute the risk of different types of injuries, depending on the impact location (Shen et al. 2012).

The ATBM is composed of models of different body regions, including the head, torso, arms, and legs. The torso is further divided into two regions, the thorax and the abdomen. Each body-region model estimates risk for a set of injuries specific to that region; for example, risk of skull fracture and brain injury are estimated for impacts to the head, while risk of arm bone fractures are estimated for impacts to the arm. The range of injuries that is theoretically possible for blunt-impact projectiles and the diversity of potential impact locations on the body mean that the computation of RSI described by Equation 1 using ATBM is further broken down to produce Equation 2:

$$RSI = \sum_{\text{body regions}} P(\text{region hit}) * P(\text{injury occurred}|\mathit{region\ hit}) * P(\text{injury significant}|\text{region hit and injury occurred}), \tag{2}$$

where, because RSI is determined based on a single hit to the body, $\sum_{\text{body regions}} P(\text{region hit}) = 1$. Equation 2 shows that understanding the distribution of hits to different body regions is an important step in the overall calculation of RSI, because certain regions of the body may be more vulnerable to significant injuries than others. In the broader context of understanding specific injury risks from blunt-impact IFCs, there may also be certain injuries that would be particularly important to avoid (e.g., fatal injuries, disfiguring injuries), so developing a detailed picture of impact distribution could be valuable beyond calculating RSI.

Past methods of estimating hit distributions in ATBM have typically assumed that the targets stand in a forward-facing posture with arms by their sides (Shen et al. 2012; Simonds et al. 2010). The distribution of hits on the body is then determined based on some knowledge of the aim point[2] and dispersion characteristics of the weapon against this posture. However, actual distribution of hits to the body in real-world scenarios will depend on many factors, including not only the aim point and accuracy and dispersion characteristics of the weapon but also the target's posture, orientation relative to the weapon, and geometry (Mezzacappa et al. 2018). Impacts from blunt-impact weapons do occur outside the aim region, and these can cause serious injuries (Olson et al. 2020).

[2] Common aim points for blunt-impact IFCs include the center of mass, the belt buckle, or the center of the torso.

Depending on the target's response to the event, certain regions of the body may become more exposed while other regions are more protected. This change in the distribution of hit locations has the potential to affect the aggregate RSI estimate.

Different people with different intentions will react differently to IFC targeting (Mezzacappa, et al. 2018). For example, a bystander may choose to duck-and-cover or run away, while a hostile actor may attempt to charge the facility being protected or the forces using the IFCs. The behavior of the target has the potential to affect the RSI. These dynamics are important to consider when determining how to responsibly use blunt-impact IFCs.

In the work described here, we first determine how defensive postures change the probability of hit (p(hit)) to different body regions by simulating hit distributions against a database of segmented images of volunteers engaged in defensive postures. Then, we apply hypothetical posture distributions to explore how such changes in p(hit) can be expected to affect calculation of RSI.

2. Methods

A. Image Collection

Using a Microsoft Kinect V2 sensor and the Image Acquisition Toolbox for Matlab, we collected images of 26 volunteers recruited from the staff of the Institute for Defense Analyses in 13 specified defensive postures. Both depth and color images were collected with concurrent computer tracking of skeleton joint positions. Subjects also self-reported their heights for use determining scale in the collected images.

All participants in the study volunteered after being informed of the intended use of the images and data-collection procedures. IDA management determined that this voluntary participation, with verbal consent from the subjects, qualified for a Human Subjects Research exemption pursuant to 45 CFR 46.104(d)(3), and therefore no Institutional Review Board was required. Data were recorded in an anonymized way, and image segmentation procedures reduced all images acquired to solid-color segmented images, which prevents any identification of facial features.

Before collecting images, each subject was briefed on the procedure that would be followed during data collection. Subjects were asked to remove any reflective items, secure loose hair or clothing, and remove bulky outer layers before the images were collected, as these could interfere with the Kinect sensor. Subjects were then briefly instructed on the general postures they would be asked to assume. Rather than requiring subjects to exactly imitate specific poses (e.g., by trying to copy images), subjects were given limited instruction, such as “protect your head” or “crouch,” to preserve natural variation in their behaviors. Subjects were instructed to think of the camera as the firing weapon during this image collection; however, no projectiles were actually sent toward the subjects. Markers were set on the floor for subject foot placement for forward-orientation and 45° turned orientation poses.

The postures requested were designed to cover three key postural variables (orientation relative to the camera, upright/crouched, and arm position) in all possible combinations. One posture representing the subject running away from the camera was also included. The postures are defined in Table 1 and Table 2. Each subject cycled through the 13 postures twice, in randomized order. One researcher was assigned to watch the Kinect skeleton tracking in real time. If it appeared that the Kinect sensor had lost track of a subject’s limbs or head during image collection, the pose was repeated. This happened most often when subjects’ arms were in protect-the-torso position. The researchers were not 100% successful in catching these skeleton-tracking errors. This source of error is discussed in Section 2.D.

Table 1. Pose Descriptions

Pose Number	Orientation	Upright/Crouched	Arm Position	Running Away
1	Forward	Upright	Unspecified	No
2	Forward	Upright	Protecting Torso	No
3	Forward	Upright	Protecting Head	No
4	Forward	Crouched	Unspecified	No
5	Forward	Crouched	Protecting Torso	No
6	Forward	Crouched	Protecting Head	No
7	Turned 45°	Upright	Unspecified	No
8	Turned 45°	Upright	Protecting Torso	No
9	Turned 45°	Upright	Protecting Head	No
10	Turned 45°	Crouched	Unspecified	No
11	Turned 45°	Crouched	Protecting Torso	No
12	Turned 45°	Crouched	Protecting Head	No
13	—	—	—	Yes

Table 2. Pose Variables

Orientation		Upright/Crouched		Arm Position		
Forward	Turned 45°	Upright	Crouched	Unspecified	Protecting Torso	Protecting Head
					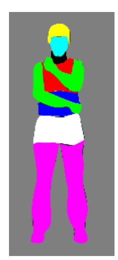	

This set of postures was determined with the objective of creating a sort of basis set for target responses to IFC. The three main variables (orientation, upright/crouched, and arm position) were determined based in part on a past study that characterized some typical behaviors in an experiment where subjects were actually subjected to paintball fire while attempting to approach the area from which the paintballs were fired (Mezzacappa et al. 2018). While the postures in Table 1 may not all be realistic responses in every situation, the goal was to attempt to build a dataset with enough control over postural variation to ascertain how distinct types of reactions might affect p(hit) distributions.

A few additional details are relevant with respect to subject arm position instruction. First, "unspecified" arms generally meant the arms were loosely by the subjects' sides in upright poses (1 and 7) intended to represent neutral or nondefensive posture, but in crouched poses (4 and 10) subjects were instructed to consider acting "like they were about to run," so arms were typically at the sides but bent at some angle. Also, subjects were asked to leave the midline of the face exposed when "protecting the head" (poses 3, 6, 9, and 12). This was to facilitate the Kinect sensor being able to track the head and to ensure that the image-segmentation algorithm would accurately mark the position of the subject's head, rather than mistakenly tagging the hands or arms as head.

B. Image Segmentation

Depth images collected by the Kinect sensor were sent through an automated image-segmentation algorithm that marked each pixel of the image as one of eight body regions—skull, face, neck, thorax, abdomen, arms, pelvis, and legs[3]—or background. Depth images were chosen for segmentation because they can simplify background subtraction, minimize the effect of clothing color patterns and scene illumination on segmentation outcomes, and detect object shape in a way that is conducive to body-part segmentation (Chen, Wei, and Ferryman 2013; Hynes and Czarnuch 2018). The image-segmentation algorithm is described here.

First, images and joint-tracking data collected by the Kinect sensor using the Matlab Image Acquisition Toolbox were converted to formats that could be read using Python code. This process involved identifying the pixel positions and associated depth value of each tracked joint in the acquired image and saving all images in Portable Network Graphics (.png) format. In addition, an image was produced that tracked which pixels in the depth image were part of the subject's body. The resulting image was effectively a silhouette of the subject. The procedure used to generate this silhouette image encountered some challenges separating the floor from the feet. The consequence was that the area of the feet in final segmentation was sometimes disproportionately large. However, because aim points are typically the center of the torso or the belt buckle position (far from the feet in most postures), this error was not expected to have much effect on the final analysis. 0 has additional information about the separation of the silhouette image from background.

The depth image, joint positions, and silhouette image were then imported into Python. Using the skimage package, the joint positions were connected using anatomical knowledge to form "axes" that would be used as seeds for the segmentation of different body regions in the depth image (see Figure 1). For example, to seed the arm regions, each arm was seeded separately by connecting the hand "joint" to the wrist, the wrist to the elbow, and the elbow to the shoulder. Table 3 describes the seeds used for each body region in the image. Axes were determined in three dimensions (horizontal, vertical, and depth)

[3] The eight regions divide the body into anatomically distinct segments with separate injury types. The regions align with region-specific injury models used or planned by JIFCO (Shen et al. 2012).

to enable determinations of overlap. When one axis was projected in front of another axis (e.g., when arms are protecting the torso), the forward axis would gain precedence in seeding the image. Note also that different seeding was used for the thorax for poses where arms were protecting the torso (poses 2, 5, 8, and 11). These poses were particularly difficult for the Kinect to track because the arms and torso overlapped, which could cause mis-seeding of the torso, arms, or both. It was determined that segmentation was more successful when the shoulder-to-center-spine axes were removed from seeding the thorax in this set of poses. Figure 1 shows examples of these two seeding approaches.

Table 3. Seed Descriptions for Image Segmentation

Body Region	Seed Description
Skull	Axis connecting highest pixel in the body above the neck position to the head "joint" position
Face	Axis connecting neck and head "joints"
Neck	Connection of neck and shoulder-spine
Thorax	For poses with arm position "protecting torso": Axes connecting shoulders and connecting center-spine to shoulder-spine For all other poses: Axes connecting shoulders, connecting shoulder-spine to center-spine, and connecting shoulders to center-spine.
Abdomen	Axes connecting base-spine to center-spine and connecting hips to center-spine
Arms	Axes connecting shoulder, elbow, wrist, and hand
Legs	Axes connecting hip, knee, and ankle
Pelvis	Triangle drawn after other segmentation completed*

* The triangle defining the pelvis was drawn between three vertices based on r_h, the distance between the hips. One vertex is at the height of the left hip, but 50% of r_h to the left. The second vertex is at the height of the right hip, but 50% of r_h to the right. The final vertex is at the horizontal position of the base-spine, but displaced 50% of r_h down.

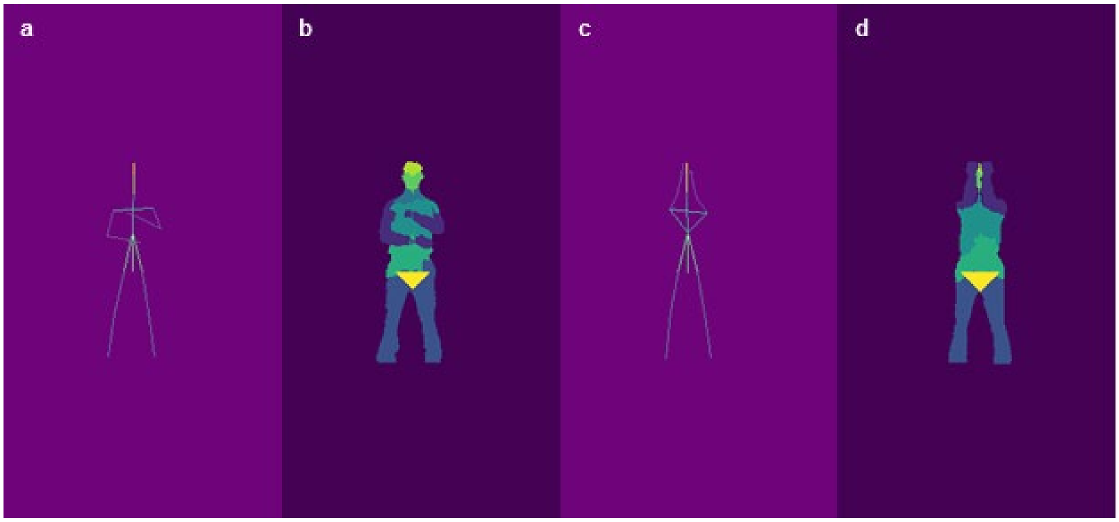

Figure 1. Examples of Axis Seeding and Segmented Images. Pose 2 axis markings (a) use less seeding of the thorax, resulting in segmented image (b). Pose 3 axis markings (c) result in segmented image (d). Both segmented images have had pelvis region added in post-processing after watershed segmentation.

After seeds were determined for each body region, the silhouette image was used to filter those seeds to only include locations that were actually on the body silhouette. Then, a watershed algorithm using the Sobel method of computing gradients (implemented using the scikit-image package in Python (van der Walt et al. 2014)) was used to segment the depth image, with the seeds for each body region as listed in Table 3 (except for the pelvis). The pelvis was added as a triangle onto the image after this watershed segmentation was completed, allowing for overlap of the arms. This was necessary because the pelvis is not a well-distinguished region like the arms or head, which can be easily identified by watershed segmentation. Figure 1 shows examples of final segmented images for poses 2 and 3.

C. Hit Distribution

With the final set of 676 segmented images, we calculated *p*(hit) distributions for each body region for a series of aim points and weapon-dispersion characteristics. The scale of each image was determined based on the associated subject's self-reported height in pose 1, when the subject was standing upright. For each aim point and weapon dispersion, projectile-impact locations were modeled using a two-dimensional normal distribution centered at the aim point with specified horizontal and vertical standard deviations (in meters). These estimates did not account for skewness in hit distributions due to parabolic trajectories, gravity, or elevation differences between the shooter and the target because we assume that such skewness is negligible as applied to overall hit distributions on body regions. We considered 10 values each for the horizontal and vertical standard deviations and modeled all 100 combinations thereof. We utilized two aim points, the center-spine “joint” and the base-spine “joint.” These positions are representative of two common aim points used in training with blunt-impact weapons, the center of the torso and the belt buckle.

We used a Monte Carlo approach to evaluate the distribution of hit locations. A set of 10,000 dimensionless hit locations (x and y positions represented as z-values[4]) were randomly generated from the standard normal distribution.[5] These 10,000 z-value pairs were used for all aim points and weapon-dispersion characteristics. The hit locations were scaled to each pair of horizontal and vertical standard deviations and overlaid on the images relative to a specified aim point to identify which body segment would be impacted by each shot.

For each image, aim point, and weapon dispersion, the segmented body region (one of the eight body regions or the background) was determined for each hit location. Total hits to each body region over the 10,000 hit locations were summed for each image. In this report, p(hit) is defined as the relative probability of hit on a body region given a hit somewhere on the body and is computed as:

$$p(\text{hit})_b = \frac{\text{number of hits on body region } b}{\text{total number of hits on the body}}. \tag{3}$$

We also computed the absolute probability of hit, P(hit), denoted with a capital P, which is not normalized by the total probability of hit anywhere on the body:

$$P(\text{hit})_b = \frac{\text{number of hits on body region } b}{\text{total number of shots}}. \tag{4}$$

We calculated statistics on these values across the 52 images in each pose and generated look-up tables for average p(hit) and P(hit), standard error of average p(hit) and P(hit), and standard deviation of p(hit) and P(hit) as a function of body region, pose, aim point, and weapon dispersion.[6] Each value in these lookup tables represented the average, standard error of the average, or standard deviation of p(hit) or P(hit) for 52 images constituting 26 subjects engaged in each pose twice. Appendix A gives the detailed mathematical derivation of the estimated mean, standard deviation, and standard error of p(hit) and P(hit) for each body region and pose.

---

[4] The standard normal distribution has mean 0 and standard deviation 1. Values pulled from the standard normal distribution are known as z-values and are equivalent to the number of standard deviations away from the mean (±) for that draw. Z-values can be rescaled to absolute values x or y for any normal distribution with mean μ and standard deviation σ by using the equation: $x = \mu + z*\sigma$.

[5] 10,000 was a computationally tractable number of points for which the results did not noticeably change from one Monte-Carlo run to another.

[6] We did not compute covariances. Because a shot that hits one body part cannot also hit another, the values for the different regions are not independent.

For the analysis in this report, we focus on two weapon-dispersion characteristics approximately representative of the 40 mm HEMI[7] round at 40 m and 100 m range (Webber et al. 2012). These are intended to concisely represent short- and long-range engagements for a common projectile launcher. At close range (40 m), the weapon dispersions were set to 0.1 m and 0.15 m for horizontal and vertical standard deviations, respectively. At long range (100 m), these values were set to 0.25 and 0.4 m, respectively. We also focus mostly on trends observed for the center-torso aim point, but many of the trends observed for this aim point are consistent for the belt-buckle (base spine) aim point. We comment when this is not the case.

Finally, plots and discussion in this report, unless otherwise stated, report relative *p*(hit) (probability that a particular body region was hit given that a hit occurred) rather than absolute *P*(hit) (probability that a body region was hit when a blunt-impact projectile was fired). *p*(hit) is readily computed by dividing *P*(hit) for a body region by *P*(hit) for the whole body (see Appendix A). Data are presented in this way because typical operational training for use of a blunt-impact projectile weapon would be to continue firing until the target has been hit.[8] Therefore, RSI is estimated on a per-hit basis.

For overall understanding of weapon performance, the absolute *P*(hit) still matters, because it determines how effectively a weapon can be used in different situations. Trade-offs between the accuracy and cost of a weapon should be considered when designing and acquiring blunt-impact IFCs. But for this analysis, which is focused on computing RSI, we assume that the target has been hit by the projectile.

D. Segmentation Errors

The automated segmentation algorithm used in this analysis was imperfect. Some challenges with automated segmentation arose from inaccuracy in the Kinect tracking of joint position, while others arose from uncertainties in the watershed-segmentation approach:

- Failure to fully separate feet from the floor, resulting in overestimates of leg region area.
- Failure to accurately distinguish face, neck, and skull regions.

---

7 The long-range, long-duration, untethered Human Electro-Muscular Incapacitation (HEMI) munition has been a long-sought and currently unmet need. Currently, all the Services field a version of the TASER International (now Axon) X-26 Taser. This device is configured in a pistol-like form factor, the cartridge is wire tethered (which limits the range and accuracy to a single human target at < 20–25 feet) and limits the non-lethal electro-muscular disruption (EMD) disable effect (i.e., full-body tetanization of the muscles) and the duration of non-lethal disable effect to 5 seconds. However, TASER International developed a 40 mm HEMI round that went through Human Effects Assessment characterization, including an assessment of weapon accuracy, as reported in Webber (2012).

8 Personal correspondence, Wesley Burgei, JIFCO.

- Kinect failure to accurately capture arm position, resulting in mis-seeding of watershed segmentation, particularly in arm and thorax region.

The first of these errors is expected to produce minor errors in p(hit) distributions because the aim point is typically far from the feet. The largest errors due to this issue will occur at long range for the belt-buckle (base spine) aim point. The second of these errors was effectively neglected in the analysis that follows by the decision to aggregate the face, neck, and skull regions into one body region called the head region. This decision sidesteps the lack of validated ATBM injury models for the neck and face. Because the face-skull-neck region is expected to be particularly vulnerable to significant injuries as a whole (Simonds et al. 2010) when exposed to blunt-impact projectiles intended for torso impact, large deviations between them would not be expected. The third source of error, the overlap of arms and torso, is of most concern for our analysis because of potential differences in the vulnerability of these body parts and because, due to their proximity to the aim point, they are most likely to be impacted.

We attempted to estimate auto-segmentation error by conducting a sensitivity study using a manually segmented subset of the images. The Kinect sensor collected color images simultaneously with depth images during data collection, but the color images had a slightly different perspective and resolution than the depth images. The Kinect also tracked joint positions in both the color images and depth images, so it was a straightforward matter to spatially register the depth and color images with each other and compute pixel/meter scale conversions. Once this had been done, we chose a subset of the images, 26 of the color images spanning all subjects and poses (1 image per subject, 2 images per pose, with pose selection randomly distributed among the subjects) and manually segmented them using ImageJ (Schneider, Rasband, and Eliceiri 2012). Table 2 shows some examples of manually segmented images, though with the pelvis region treated differently than in the final image set. We then ran these manually segmented images through our p(hit) simulation side by side with the corresponding auto-segmented images.

For each image, body region, aim point, and weapon dispersion, we quantified the difference in relative p(hit) computed for the auto-segmented image (p_{auto}(hit)) and the manual image (p_{manual}(hit)). We then averaged the differences between p_{auto}(hit) and p_{manual}(hit) to estimate the average difference between auto and manual segmentation for each pose and body region (including the whole body) by summing over the two subjects per pose according to Equation 5:

$$\hat{p}_{\text{diff}} = \frac{1}{2}\sum_{\text{subjects}}^{2} p_{\text{auto}}(\text{hit}) - p_{\text{manual}}(\text{hit}). \quad (5)$$

Appendix A has additional detail on this calculation. Figure 2 plots $\hat{p}_{\text{diff}}$ as a function of pose and effective HEMI range for the center sternum aim point. The magnitude of overall $\hat{p}_{\text{diff}}$ values is usually largest for the abdomen and thorax because these large regions close to the aim point are the most likely to be hit, particularly at close range.[9] $\hat{p}_{\text{diff}}$is typically small for the head, partly because the actual p(hit) for the head is already small, since this region is neither large nor close to the aim point.

For a number of the body regions and poses, the $\hat{p}_{\text{diff}}$ results have the character of *bias*, rather than unbiased uncertainty. That is, the deviation in $\hat{p}_{\text{diff}}$ is small relative to the actual value of $\hat{p}_{\text{diff}}$ for those pose-body region conditions. This is most easily identified in examples where the error bars (representing standard error of our estimate of $\hat{p}_{\text{diff}}$ based on two images per posture) in the figures stay far from crossing the x-axis. Such systematic bias will be considered in our broader analysis of overall p(hit) distributions and discussed further in Appendix A. For such a small sample size (two images) per pose, there is little that can be confidently inferred statistically from the pose-by-pose data.

Looking across poses and exploiting forensic examination of the individual image segmentations allow us to make more qualitative observations about the auto-segmentation. For the center-torso aim point, auto-segmentation overestimates p(hit) to the head, abdomen, and thorax for most poses, while auto-segmentation typically underestimates p(hit) to the legs, arms, and pelvis.[10] Most errors are under 10% in terms of relative p(hit), with notable exceptions—p(hit) to the arms is often underestimated when the arms overlap the torso significantly (poses 2, 5, 8, and 11). This is typically compensated by overestimates of p(hit) in the thorax and/or the abdomen. This error reflects the challenges with segmentation based on Kinect tracking of arms in front of the torso. Some errors in p(hit) estimation for abdomen vs. thorax can be attributed to differences in how the human analyst visually identified the boundary between thorax and abdomen vs. how the Kinect makes this judgment (referenced to the center-spine "joint" position). Errors in poses 4 and 11 in distinguishing between legs and abdomen are attributed to difficulty the Kinect has in identifying the position of the hips in crouched poses, particularly pose 11. Finally, the triangle method of identifying the pelvis results in general underestimation of the pelvis for the running-away pose, for which the pelvis

---

[9] For the belt-buckle aim point, the largest deviations are for the abdomen and legs, for similar reasons. See Figure C-1.

[10] For the belt-buckle aim point, auto-segmentation typically overestimates p(hit) to the abdomen and underestimates p(hit) for the legs and pelvis, with very small estimation errors observed for the arms, head, and thorax (the regions least likely to be hit) (see Figure C-1). Errors for the arms, legs, head, and pelvis are typically under 5%. At close range, the abdomen p(hit) is typically overestimated by 15% to 30%, but the legs experience the opposite effect; this difference is likely due to the difficulty of auto-segmentation distinguishing the boundary between the leg, pelvis, and abdominal regions that are all close to the aim point. The magnitude of these errors decreases at longer range to typically below 15%. Poses 11 and 13 show particularly severe errors in p(hit) estimation for legs and abdomen—at close range, errors as large as –60% are observed for the legs for pose 11 (compensated by overestimates of p(hit) for both the abdomen and thorax), while at long range this error is within –30%. Identifying the pelvis region was a particular challenge for the auto-segmentation with pose 11.

projects more of a trapezoidal shape.[11] Appendix A has more discussion on the analysis of segmentation error.

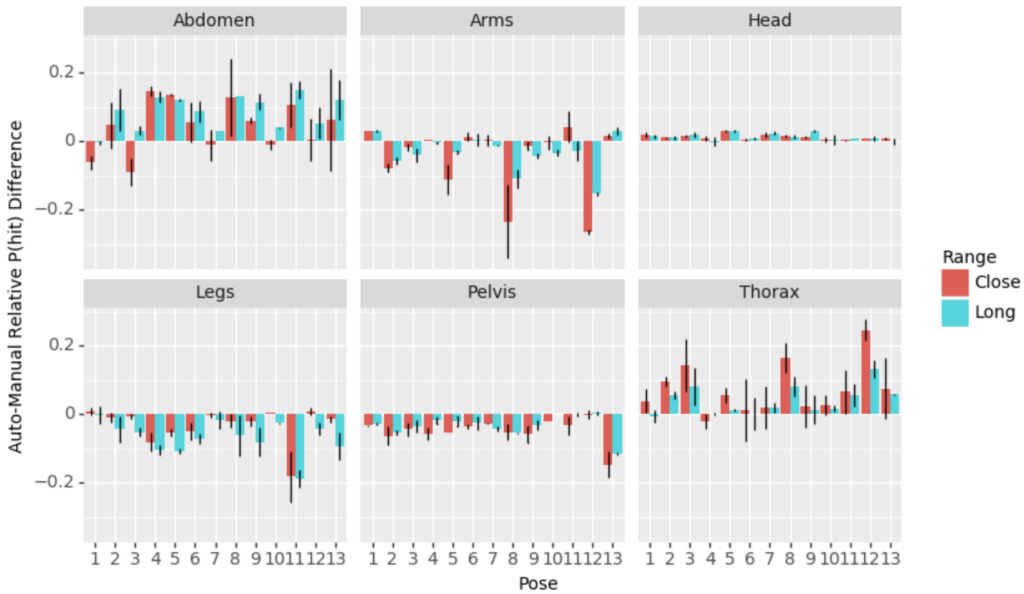

Figure 2. Average Differences in Relative *p*(hit) between Auto-segmented and Manually Segmented Images ($\widehat{p}_{\mathrm{diff}}$) for Center-Sternum Aim Point. Bar color indicates 'close' and 'long' range weapon dispersion patterns. Error bars indicate standard error of the difference computed in this way for two images.

[11] These issues for poses 11 and 13 are exacerbated for the belt-buckle aim point.

3. Postural Effects on *p*(hit)

We next examine how various postural changes affect the hit distribution on the target. Using the results of the simulations described in Section 1 we analyze postural change effects. Our data collection allows us to consider five general types of defensive reactions, as summarized in Table 4. We will consider each of these reactions separately. These effects are examined based on pose pairs, where all pose features (orientation, upright/crouched, arm position) are held constant *except* for the action of interest. For example, the pose pair (1, 3) explores the "protect head effect" because the subject is standing upright and facing forward for both pose 1 and pose 3, but in pose 1 the arms are unspecified while in pose 3 the arms are protecting the head. Due to the finite flight time of a blunt-impact projectile, there may be time for a target to react defensively between the aiming of the weapon and the impact of the projectile. We treat each pose as if it were assumed upon awareness of the threat and before aiming. For example, a center-sternum aim point will produce a distribution of hit locations centered on the center-sternum of the target in the defensive posture. There are certainly other reasonable assumptions for analysis of defensive posture effects.

Where applicable, we also consider auto-segmentation biases with respect to the *transition* that we are interested in. For a transition from pose **A** to pose **B**, if both poses have similar auto-segmentation bias, we do not expect the observed change in *p*(hit) to be strongly affected. However, if pose **A** and pose **B** have very different auto-segmentation bias (for example, pose **A** is close to unbiased, but pose **B** is typically underestimated by several percentage points), then auto-segmentation bias has the potential to either over-emphasize or mask a real effect.

Note again that the figures in this section reflect relative *p*(hit) for the center-torso aim point. Where applicable, we discuss how trends for a belt-buckle aim point differ from trends for the center-torso aim point.

Table 4. Summary of Defensive Actions and Associated Pose Pairs

Defensive Action	Description	Pose Pairs (start, end)
Crouch	Moving from an upright position to a crouched or ducked position	(1, 4), (2, 5), (3, 6), (7, 10), (8, 11), (9, 12)
Turn	Moving from facing the weapon to partial profile (45°) relative to the weapon	(1, 7), (2, 8), (3, 9), (4, 10), (5, 11), (6, 12)
Protect Head	Moving the arms to shield the head from impact	(1, 3), (4, 6), (7, 9), (10, 12)
Protect Torso	Moving the arms to shield the thorax or abdomen from impact	(1, 2), (4, 5), (7, 8), (10, 11)
Run Away	Turning away from the weapon and running	(1, 13)

A. Crouch

Moving from an upright position to a crouched position has several consequences. First, crouching can reduce the total projected area of the body. For low-accuracy weapons, this translates to a reduction in absolute *P*(hit) per shot. Second, crouching or ducking brings the extremities and the head closer to the aim point. Finally, crouching can cause certain portions of the body to project in front of other portions of the body.

Figure 3 summarizes the effect of crouching for the six pose pairs listed in Table 4. On average, crouching decreases the estimated relative *p*(hit) to the abdomen and thorax and increases estimated relative *p*(hit) to the legs and arms. Small positive changes are also observed for the *p*(hit) estimated for pelvis and head, which have a fairly small expected *p*(hit) to start with. However, given that the head is expected to be a more vulnerable region of the body than other regions, even a few percentage points of increased *p*(hit) to the head could translate to a large increase in the total RSI. Crouching or ducking is therefore effective at reducing relative *p*(hit) to the torso (*p*(hit) to the abdomen reduced by up to one-third, *p*(hit) to the thorax reduced by up to one-fifth), at the expense of other regions of the body.

Our analysis of segmentation error suggested that the *p*(hit) to the abdomen is typically *overestimated* by auto-segmentation for poses 4 and 5, while *p*(hit) to the legs is typically *underestimated*. These results suggest that the actual changes in *p*(hit) to the abdomen and legs are larger than the estimate derived from the auto-segmentation dataset. In other words, the effect size for the abdomen and legs is probably larger than suggested by Figure 3.

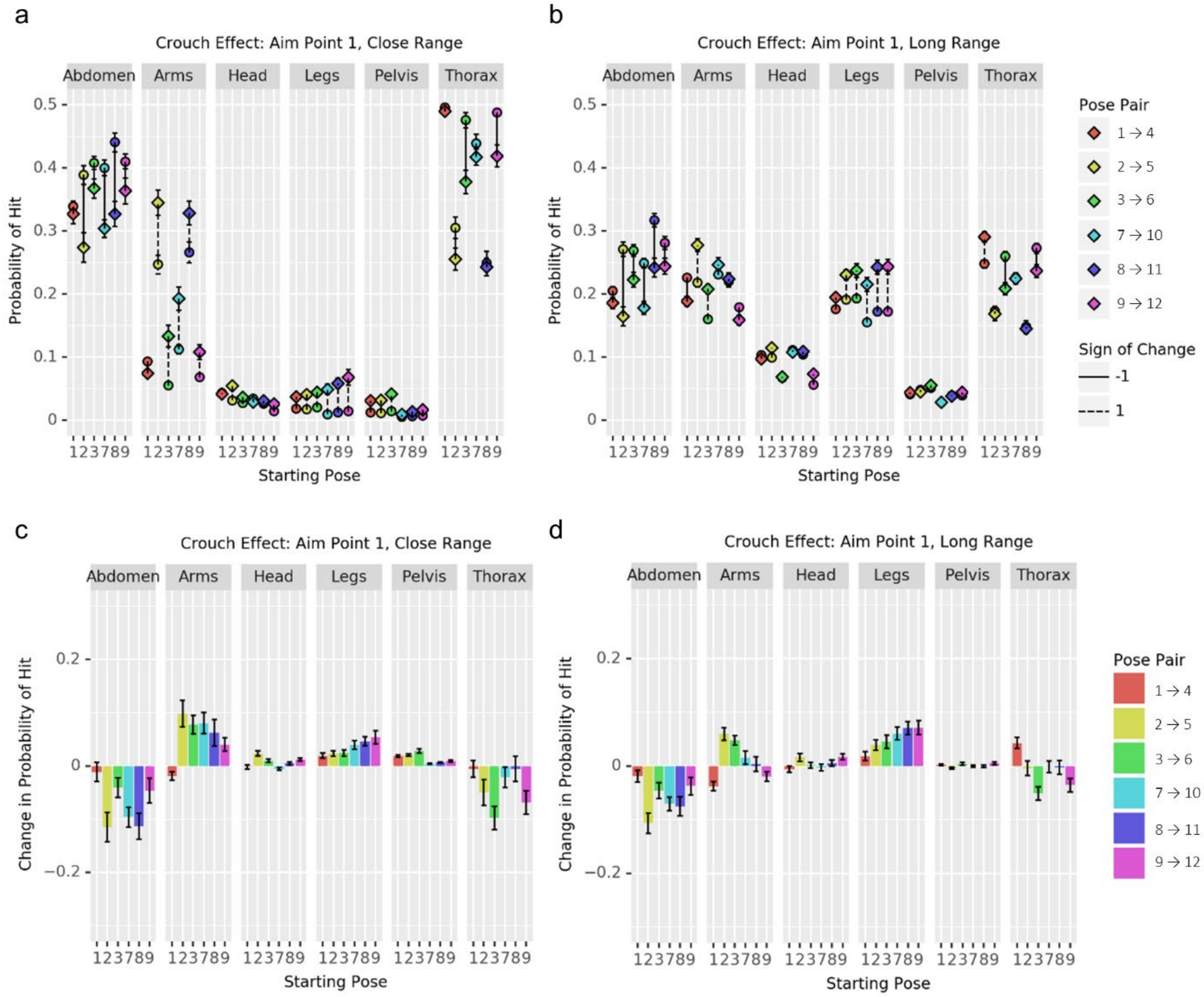

Figure 3. Changes in Relative *p*(hit) Distribution Across Six Body Regions for Crouch Action. These plots correspond to the center-torso aim point (Aim Point 1), with data aggregated across 52 images for each posture and body region. Color represents the starting posture in transitions defined in Table 4. (a, b) Relative *p*(hit) before (circles) and after (diamonds) the subject crouches for (a) short-range and (b) long-range weapon dispersion. Solid lines indicate that crouching decreased *p*(hit) for that starting posture and body region. Dashed lines indicate that crouching increased *p*(hit). Error bars represent standard error of the mean for starting and ending expected *p*(hit). (c, d) Change in relative *p*(hit) for crouch posture pairs for (c) short-range and (d) long-range weapon dispersion. Error bars represent standard error of the mean for change in *p*(hit).

Overall, these results fit expectations because crouching or ducking moves the legs, arms, and head closer to the aim point, potentially simultaneously blocking the thorax and abdomen.

The trends observed for the belt-buckle aim point differ from those observed for the center-sternum in that the relative *p*(hit) to the legs *decreases* for all forward-facing poses while the relative *p*(hit) to the thorax typically increases, as shown in Figure 4. This is the case because the belt-buckle aim point, in the absence of defensive action, is dominated by impacts to the legs and abdomen, while impacts to the thorax and abdomen dominate for the center-torso aim point. When targets crouch, they project their thorax closer to the belt-buckle aim point and also typically shrink the projected area of the legs. So, when the aim point is the belt buckle, the proportion of impacts that hit the thorax increases relative to the legs.[12] When the aim point is the center of the torso, crouching instead increases the relative p(hit) to the legs and decreases the relative p(hit) to the thorax and abdomen.

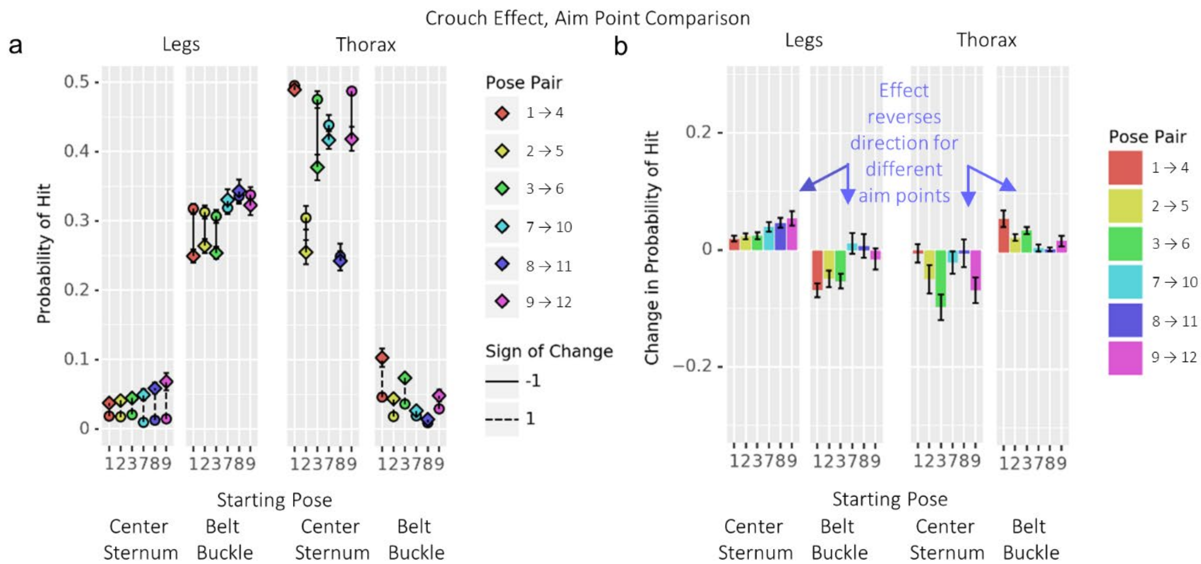

Figure 4. Comparison of Crouch Effect for Two Aim Points at Close-Range Weapon Dispersion. Color represents the starting posture in transitions defined in Table 4. (a) Relative *p*(hit) before (circles) and after (diamonds) the subject crouches. Solid lines indicate that crouching decreased *p*(hit) for that starting posture and body region. Dashed lines indicate that crouching increased *p*(hit). Error bars represent standard error of the mean for starting and ending expected *p*(hit). (b) Change in relative *p*(hit) for crouch posture pairs. Error bars represent standard error of the mean for change in *p*(hit).

B. Turn

The action of turning is more complicated to analyze than the action of crouching. Our dataset included images in partial profile (feet facing at a 45° angle relative to the camera). Figure 5 shows that turning has a lot of interaction with the other defensive actions (arm position, crouching). This results in pose-dependent variability in the observed changes in p(hit) distributions. This also means that the direction of change in p(hit) is uncertain in many cases.

[12] Note, however, that segmentation error, particularly at close range, may cause the effect size for the legs to appear larger than it actually is. See Figure C-1.

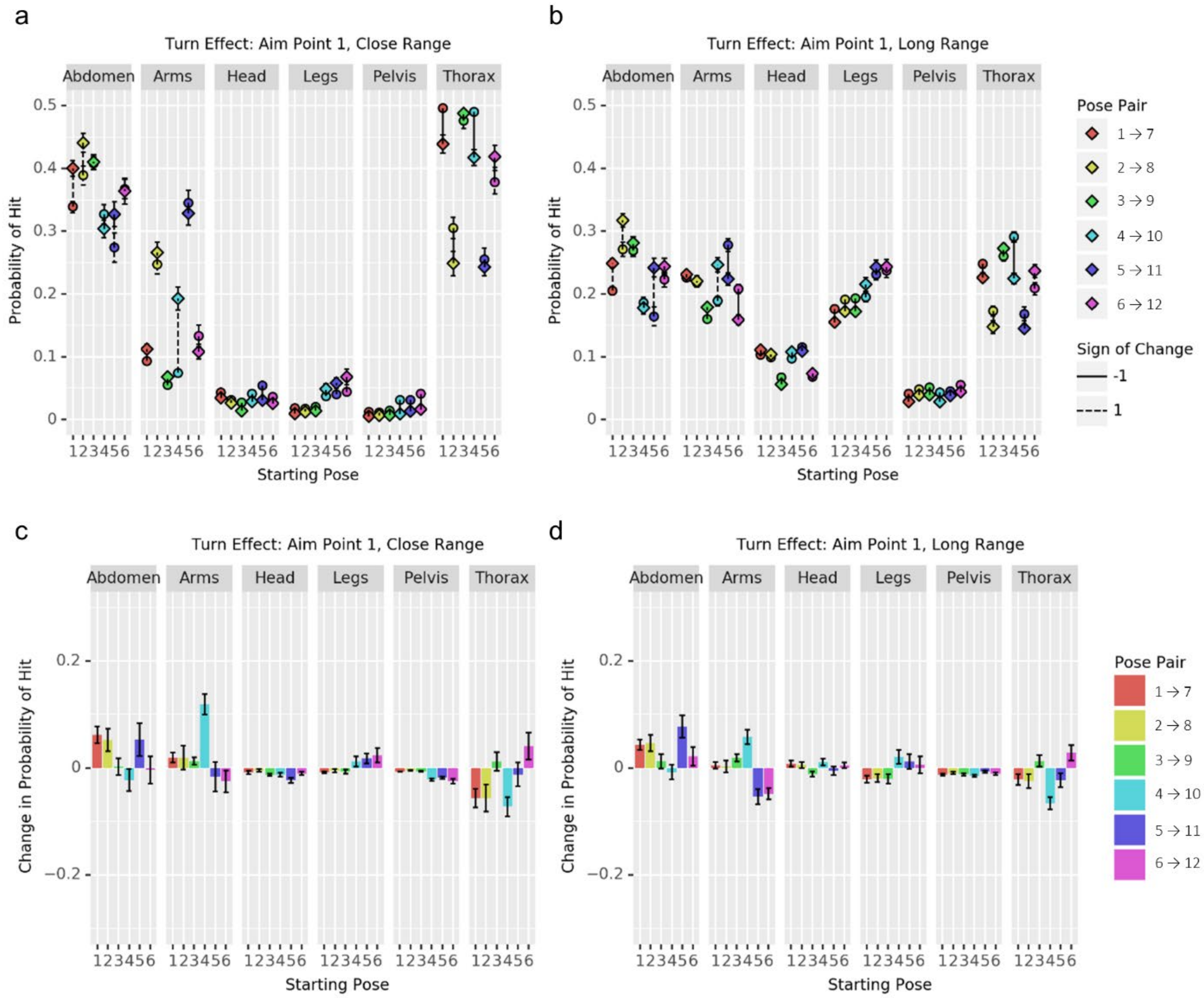

Figure 5. Changes in Relative *p*(hit) Distribution Across Six Body Regions for Turn Action. These plots correspond to the center-torso aim point (Aim Point 1), with data aggregated across 52 images for each pose and body region. Color represents the starting posture in transitions defined in Table 4. (a, b) Relative *p*(hit) before (circles) and after (diamonds) the subject turns to a 45° partial profile relative to the camera for (a) short-range and (b) long-range weapon dispersion. Solid lines indicate that turning decreased *p*(hit) for that starting posture and body region. Dashed lines indicate that turning increased *p*(hit). Error bars represent standard error of the mean for starting and ending expected *p*(hit). (c, d) Change in relative *p*(hit) for turn posture pairs for (c) short-range and (d) long-range weapon dispersion. Error bars represent standard error of the mean for change in *p*(hit).

Turning 45° typically reduces the cross-sectional area of the thorax and pelvis, but does little to affect the cross-sectional area of the head. This explains why the *p*(hit) observed for pelvis and thorax show decreases with turning in most cases. Turning while crouched typically *increases* the cross-sectional area of the legs, causing a small increase in relative *p*(hit) to the legs for poses 4, 5, and 6. In some subjects, however, turning can also *increase* the cross-sectional area of the abdomen relative to the thorax (especially in crouching positions), leading to an overall increase in relative *p*(hit) to the abdomen.

At the same time, the arm position will strongly affect relative *p*(hit). Subjects had varied reactions to the instructions "protect the torso" or "protect the head." Some subjects put their hands in front of their bodies in the direction of the camera, while others engaged in "self-hugging" behaviors, where their limbs were tucked around the head or the torso. Self-hugging typically protects the thorax; projecting the hands forward can protect the abdomen, especially if the subject is also crouched. Figure 5 shows that turning decreased *p*(hit) to the arms for poses 5 and 6, but increased *p*(hit) for pose 4. We reason that the increase for pose 4 results from the arm in "unspecified" position occupying a larger fraction of the torso's cross-sectional area when in partial profile. The decreased arm *p*(hit) for pose 5 is explained by a decrease in the cross-sectional area of the arms when they were protecting the torso.

The change observed for pose 6 transitioning to pose 12 is difficult to interpret because pose 12 showed a strong bias toward underestimating arm *p*(hit) and overestimating thorax *p*(hit) in auto-segmentation.

The belt-buckle aim point (see Appendix C) gave very similar results for the "turn effect," but with a stronger increase in *p*(hit) to the legs for crouched poses (4–6). The belt-buckle aim point also showed a more consistent trend toward decreased *p*(hit) to the head, although this effect was again small.

Even when turning does not change the *p*(hit) distribution across the six regions tracked in our analysis, it will change which types of injuries are most likely for each body region. For example, turning the head may leave only one eye exposed to potential impact (reducing the relative *p*(hit) for the eyes even if relative *p*(hit) for the head stays constant), while turning the torso can expose the kidneys or the spine to impact while protecting the heart. This complexity needs to be considered in aggregating risk within body regions by informing which impact locations and directions are most likely.

C. Protect the Head

As shown in Figure 6, using the arms to protect the head usually resulted in increased *p*(hit) to the abdomen, decreased *p*(hit) to the arms, and decreased *p*(hit) to the head. The effect on *p*(hit) for the legs and pelvis was a slight increase at long range, and the effect for the thorax depended on whether the subject was crouched. These results occur because protecting the head typically moves the arms away from the aim point while also projecting the arms in front of the head. So, the few hits that would normally have hit the head region now hit the arm region, but a smaller proportion of hits impact the arm region because it is no longer as close to the aim point. Overall, protecting the head is effective at its intended purpose—at long range (when the head is more likely to be hit due to weapon dispersion), protecting the head reduces p(hit) to the head by half.

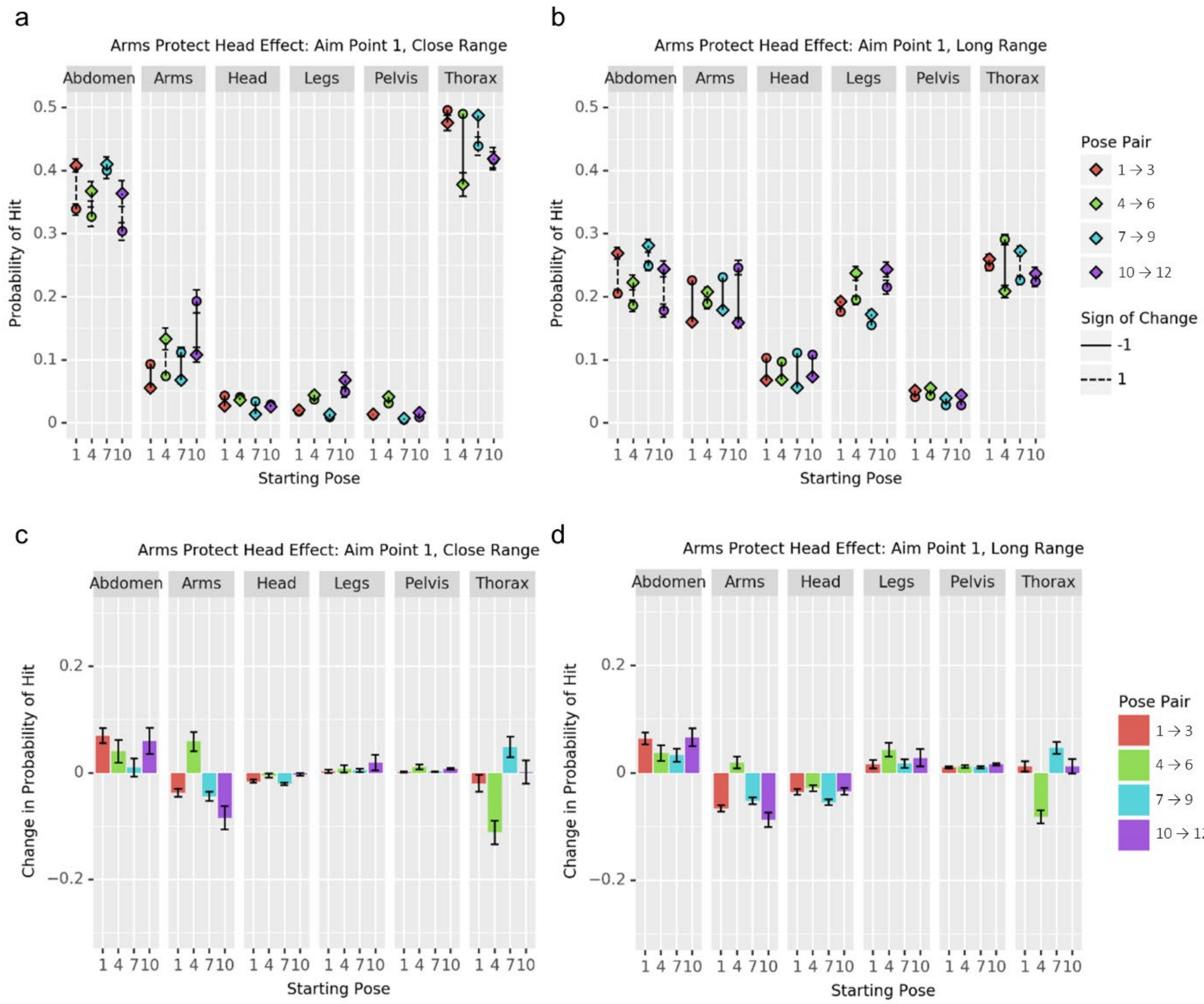

Figure 6. Changes in Relative p(hit) Distribution Across Six Body Regions for Protect Head Action. These plots correspond to the center-torso aim point (Aim Point 1), with data aggregated across 52 images for each pose and body region. Color represents the starting posture in transitions defined in Table 4. (a, b) Relative p(hit) before (circles) and after (diamonds) the subject protects the head with the arms for (a) short-range and (b) long-range weapon dispersion. Solid lines indicate that protecting the head decreased p(hit) for that starting posture and body region. Dashed lines indicate that protecting the head increased p(hit). Error bars represent standard error of the mean for starting and ending expected p(hit). (c, d) Change in relative p(hit) for "Protect Head" posture pairs for (c) short-range and (d) long-range weapon dispersion. Error bars represent standard error of the mean for change in p(hit).

In the case of the pose 10 to pose 12 transition, we note that the effects of arm and thorax p(hit) are likely *overestimated* in Figure 6 because pose 12 showed a strong bias toward underestimating arm p(hit) and overestimating thorax p(hit) in auto-segmentation. Similarly, the effect observed for the abdomen for the pose 7 to 9 transition may be an overestimate because of auto-segmentation bias toward overestimating p(hit) to the abdomen in pose 9.

The belt-buckle aim point gave similar results for protecting the head but with a stronger increase in p(hit) to the legs and a weaker decrease in p(hit) to the head.

D. Protect the Torso

As shown in Figure 7, using the arms to protect the torso results in substantial decreases in relative p(hit) to the thorax, with corresponding increases in p(hit) to the arms at close range and increases in p(hit) to the legs and abdomen at long range. This trend is explained by three facts. First, most subjects responded to the instruction to "protect the torso" by either hugging the rib cage (thorax) or projecting the hands in front of them as if to block an incoming projectile—these actions tend to increase p(hit) to the arms while reducing p(hit) to the thorax. Second, when the arms protect the torso, this typically decreases the total cross-sectional area of the body, therefore increasing the proportion of cross-sectional area occupied by abdomen and legs and resulting in increased p(hit) to the abdomen and legs. Third, auto-segmentation biases mask the size of the effects for the "protect torso" action.

In the case of the protect-torso action, we are focused on transitions (1, 2), (4, 5), (7, 8), and (10, 11). A detailed look at the auto-segmentation vs. manual segmentation data in Figure 2 shows that the (1, 2), (4, 5), and (7, 8) transitions will all be biased toward suggesting a decrease in p(hit) for the arms. Meanwhile, the (1, 2), (7, 8) and (10, 11) transitions will all be biased toward suggesting an increase in p(hit) for the abdomen, particularly at long range. Finally, the (1,2) and (7,8) transitions will be biased toward suggesting an increase in p(hit) for the thorax when the subject protects the torso.

Based on these data, we see that the final p(hit) for the arms is probably higher than what is shown in Figure 7 for poses 2, 5, and 8. At the same time, the final p(hit) for the thorax is probably less than what is shown in the figure for poses 2 and 8. Both of these facts suggest that the effect of the transition is *masked* by auto-segmentation bias. When the target "protects the torso," p(hit) for the arms likely *increases more than shown*, while p(hit) for the thorax *decreases more than shown*. Conversely, the final p(hit) for the abdomen, particularly at long range, is probably less than what is shown in Figure 7 for poses 8 and 11, so this effect is probably *smaller than shown*.

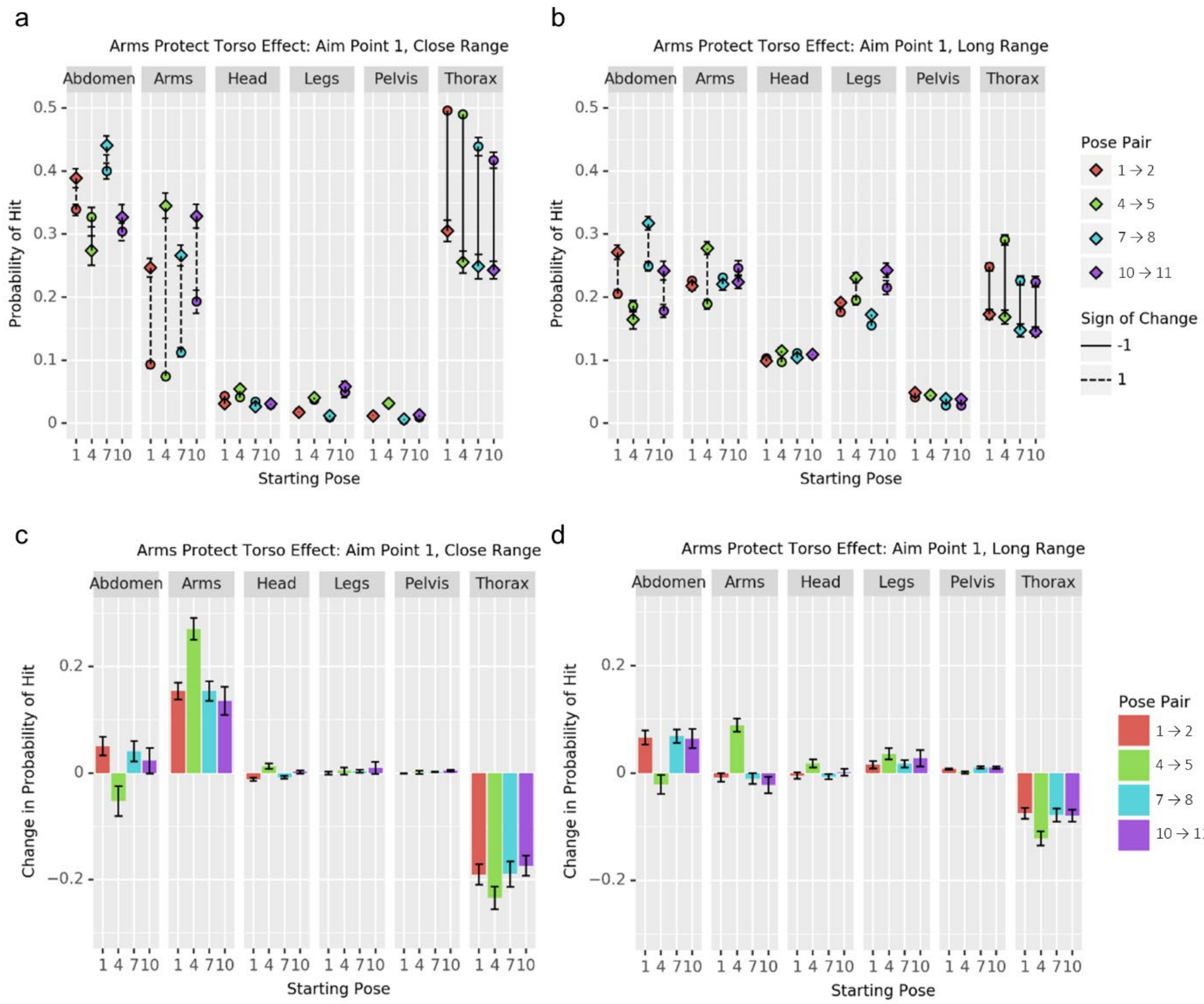

Figure 7. Changes in Relative *p*(hit) Distribution Across Six Body Regions for Protect Torso Action. These plots correspond to the center-torso aim point (Aim Point 1), with data aggregated across 52 images for each pose and body region. Color represents the starting posture in transitions defined in Table 4. (a, b) Relative *p*(hit) before (circles) and after (diamonds) the subject protects the torso with the arms for (a) short-range and (b) long-range weapon dispersion. Solid lines indicate that protecting the torso decreased *p*(hit) for that starting posture and body region. Dashed lines indicate that protecting the torso increased *p*(hit). Error bars represent standard error of the mean for starting and ending expected *p*(hit). (c, d) Change in relative *p*(hit) for "Protect Torso" posture pairs for (c) short-range and (d) long-range weapon dispersion. Error bars represent standard error of the mean for change in *p*(hit).

This analysis therefore concludes that protecting the torso typically trades impacts to the thorax for impacts to the arms. Figure 7 shows that the effect (underestimated by this analysis) can be quite large, with up to a factor of 3 change in *p*(hit) to the arms while cutting *p*(hit) to the thorax nearly in half. At long range, the relative likelihood of impacting other body regions, such as the legs and abdomen, is also modestly increased due to an increased proportion of the overall cross-sectional area of the body.

The trends observed for the center-torso aim point are consistent with those observed for the belt-buckle aim point except that the *p*(hit) to the arms decreases for all transitions except (4, 5) for both close and long range.[13] This results because protecting the thorax brings the arms away from the belt buckle most of the time. Pose 4 is an exception to this because in a face-forward crouch the thorax is quite close to the belt buckle, so protecting the torso does not bring the arms out of the aim region.

E. Run Away

Figure 8 shows that running away (transition from pose 1 to pose 13) has a small effect on the *p*(hit) distribution at close range but causes an increase in *p*(hit) to the abdomen (possibly due to auto-segmentation bias) and a decrease in *p*(hit) to the arms and head at long range. These effects result because when subjects run away, they typically lean in the direction they are running. This causes the thorax to partly shadow the head and arms and reduces the overall cross-sectional area of the thorax relative to the abdomen. In fact, running away is nearly as effective at preventing the head from being hit as protecting the head with the arms. These trends are also consistent with the results for the belt-buckle aim point, including the role of auto-segmentation bias, although auto-segmentation bias likely masks the effect of running away on the probability of hitting the legs for the belt-buckle aim point.

Like turning, running away also has the effect of changing which injuries are most likely in a given body region. When a person is running away, the skull is more likely to be hit and the face unlikely to be hit. Similarly, running away exposes the target's spine and kidneys while protecting the heart and sternum. These subtleties should be considered for determining which impact locations and directions are most important for predicting injury risk on a region-specific basis when calculating aggregate RSI.

[13] Analysis of auto-segmentation error for the belt-buckle aim point (Figure C-1) suggests that the effects on the arms and thorax are probably not significantly biased by this source of error, but that the effect for the abdomen is probably smaller than shown in Figure C-5 for the (10, 11) transition.

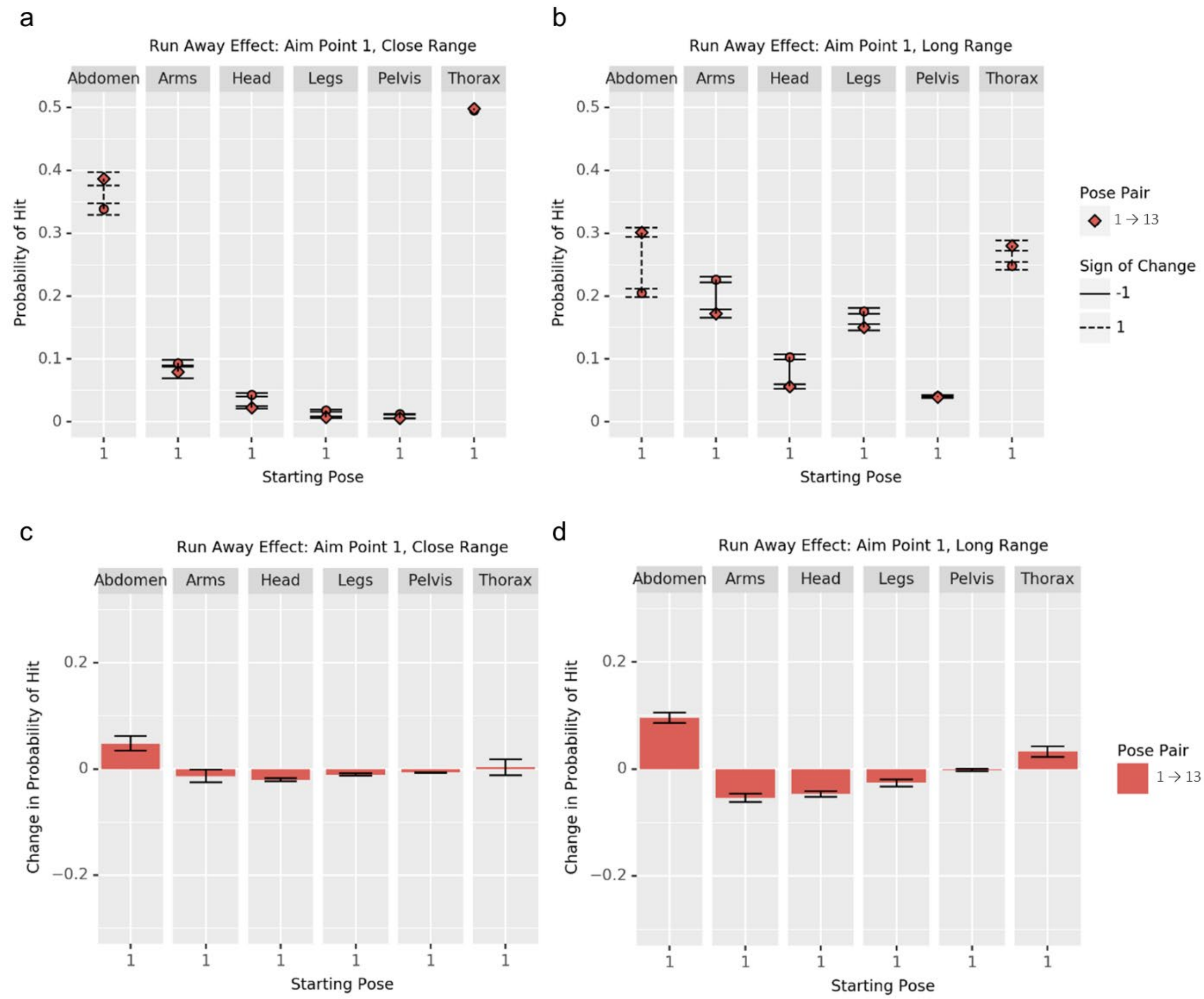

Figure 8. Changes in Relative *p*(hit) Distribution Across Six Body Regions for Run Away Action. These plots correspond to the center-torso aim point (Aim Point 1), with data aggregated across 52 images for each pose and body region. (a, b) Relative *p*(hit) before (circles) and after (diamonds) the subject runs away for (a) short-range and (b) long-range weapon dispersion. Solid lines indicate that running away decreased *p*(hit) for that body region. Dashed lines indicate that running away increased *p*(hit). Error bars represent standard error of the mean for starting and ending expected *p*(hit). (c, d) Change in relative *p*(hit) for "Run Away" posture pair for (c) short-range and (d) long-range weapon dispersion. Error bars represent standard error of the mean for change in *p*(hit).

4. *p*(hit) and RSI as a Function of Posture Distribution

The next step of our analysis is to consider how these changes in impact distribution for individual postures translate to overall RSI calculation. We compute an estimate of RSI for several representative posture distributions and body-region specific injury risks. This calculation proceeds as described in Equations (6)–(9):

$$p(\text{hit})_b = \sum_p w_p p(\text{hit})_{b,p} \tag{6}$$

where $p(\text{hit})_{b,p}$ is the probability of hitting body region b given a single hit to a person in pose p, w_p is the probability of an engagement encountering a target in pose p, and $p(hit)_b$ is the probability of hitting body region b given a single hit to a person in an unspecified pose drawn from the distribution described by $\{w_p\}$.

$$\sigma_b = \sqrt{\sum_p w_p^2 \sigma_{b,p}^2} \tag{7}$$

where $\sigma_{b,p}$ is the standard deviation of $p(\text{hit})_{b,p}$, and σ_b is the standard deviation of $p(\text{hit})_b$.

$$RSI = \sum_b p(\text{hit})_b RSI_b \tag{8}$$

where RSI_b is the probability of a significant injury given a hit to body region *b*, and *RSI* is the overall probability of a significant injury given a hit.

$$\sigma_{RSI} = \sqrt{\sum_b (\sigma_b^2 * \sigma_{RSI,b}^2 + \sigma_b^2 * RSI_b^2 + p(\text{hit})_b^2 * \sigma_{RSI,b}^2)} \tag{9}$$

where $\sigma_{RSI,b}$ is the standard deviation of RSI_b, and σ_{RSI} is the standard deviation of *RSI.*

For each posture distribution, we compute an estimated *p*(hit) for each body region *b* as well as an estimate of uncertainty σ_b. The estimated *p*(hit) for each body region is determined by a weighted sum over the *p* poses in the posture distribution following Equation 6, with standard error σ_b determined following Equation 7, where w_p is the proportion of subjects in pose *p.* Note that this method of computing uncertainty σ_b implicitly assumes that the $p(\text{hit})_{b,p}$ are uncorrelated, which we believe is a reasonable assumption (see Appendix B for more discussion), and requires that the sum of the $\{w_p\}$ is 1.

To compute aggregate RSI, we apply Equation 8, which weights the conditional probability of significant injury for impacts to each body region (RSI_b) by the p(hit) for each body region. The uncertainty for this estimate is determined from Equation 9, which implicitly assumes that the $\{p(\text{hit})_b\}$ and $\{RSI_b\}$ are uncorrelated. In reality, some correlation should exist for the $\{p(\text{hit})_b\}$ because these should sum to 1, while independence for the $\{RSI_b\}$ is more reasonable. This method of estimating error is likely to overestimate uncertainty by failing to account for any correlation that may exist (see Appendix B for further discussion).

Note that for the plots shown in this section, we set $\sigma^2_{RSI,b}$ to 0 to focus on the effects of posture-distribution uncertainty. However, in real calculations of aggregate RSI, there will be uncertainty in the estimated RSI for each body region, corresponding to nonzero $\sigma^2_{RSI,b}$. Such additional uncertainty should also be included in actual aggregate RSI calculations. This additional source of uncertainty is discussed briefly in Appendix A but is otherwise outside the scope of this report.

Table 5 describes the posture distributions we considered. These distributions try to capture a range of possible target behavior in different scenarios. For example, the "All Pose 1" distribution and the "Half-Turned" distribution represent naïve crowds (unaware of IFC targeting) with and without 50/50 orientation variation. The "TBRL-Inspired" distribution is based on the results of an experiment conducted at the Target Behavioral Response Laboratory (TBRL) (Mezzacappa et al. 2018), in which human volunteers were attempting to accomplish an aim-and-fire task while being targeted by a paintball gun.[14] The "Arbitrary" distribution represents a mix of all of the defensive postures used in our dataset with emphasis on poses 1 and 13. Finally, the "Huddle" distribution represents a case in which the entire set of subjects is engaged in mixed duck/protect torso responses while in a 50/50 mix of orientations. The "Half-Turned" and "Huddle" distributions are meant to represent the before and after behavior of a crowd of noncombatants that transition from a naïve state to trying to protect their bodies from the weapons as much as possible without running away. Based on our prior analysis of individual action effects (crouch,

[14] In the Mezzacappa et al. (2018) experiment, 20 subjects were videotaped while being fired upon by a paintball gun. The subjects were attempting to complete a task in which they were running across a room and stopping periodically to aim and fire at a target. The behaviors of each subject were tracked across several trials with varying levels of impact intensity from the gun firing at the subjects. Twenty subjects in all were tracked, and behaviors such as self-hugging, ducking down, rotating, and using the arms to block the face were observed. Often, subjects engaged in multiple behaviors in a single trial or at a single moment in time. These behaviors, though not in complete registry with our own pose set described in Table 1, were loosely possible to associate with that list. For each of the postures listed in Table 1, we counted the number of subjects in Mezzacappa et al. (2018) that engaged in similar behavior. When subjects engaged in multiple behaviors, those behaviors were divided across the subject (e.g., if a subject did something similar to pose 11 at one point and similar to pose 13 at another, then pose 11 and 13 would each be counted as 0.5 for that subject). We then computed the proportion of the 20 subjects that engaged in behaviors similar to each of the 13 postures to generate the TBRL-inspired distribution.

turn, protect head, protect torso), the combined duck and protect torso response should produce the largest differences in p(hit) distribution relative to the “Half-Turned” distribution. Of the posture distributions used for our analysis, the “All Pose 1” distribution is equivalent to the usual method of computing RSI, which does not account for orientation effects or posture effects.

Table 5. Representative Posture Distributions

Distribution Name	Distribution Description	Distribution Composition
All Pose 1	100% of subjects in Pose 1, representative of the current protocols used in RSI assessment	100% pose 1
Half-Turned	Equal mix between poses 1 and 7—representative of a naïve crowd	50% pose 1, 50% pose 7
TBRL-Inspired	Mix of poses determined based on analysis of (Mezzacappa et al. 2018), representative of a set of targets attempting to accomplish an aim-and-fire task	10% each of pose 1, 8 and 10, 5% each of pose 2, 4, 5, and 7. 25% pose 11, 7.5% pose 12, and 17.5% pose 13
Arbitrary	Mix of poses representative of an agnostic mix of our image-collection dataset, with a slight bias toward running away (pose 13)	10% pose 1, 20% pose 13, 70% uniformly divided among the other 11 poses
Huddle	Equal mix between poses 5 and 11—representative of the crowd from the “Half-Turned” distribution engaged in both ducking and protecting torso actions.	50% pose 5, 50% pose 11

Figure 9 shows the variation in relative probability of hit as a function of body region for the set of posture distributions listed in Table 5. At close range, all cases are dominated by hits to the thorax and abdomen, except the “Huddle” posture distribution, in which the arms take many more impacts while the thorax takes fewer. At long range, the p(hit) distribution is more evenly spread across the thorax, abdomen, arms, and legs for all posture distributions, and the relative p(hit) for the head, legs and pelvis is increased relative to the short-range distribution. These trends occur because at long range, the weapon dispersion covers a greater portion of the body, so regions that are farther from the aim point (head, legs, pelvis) get hit more often than they did at close range. This is compensated by a decrease in the relative impact frequency to the thorax and abdomen. Another way to think of this is that as the dispersion of the weapon increases, p(hit) distributions increasingly resemble the proportional cross-sectional area of each body region.

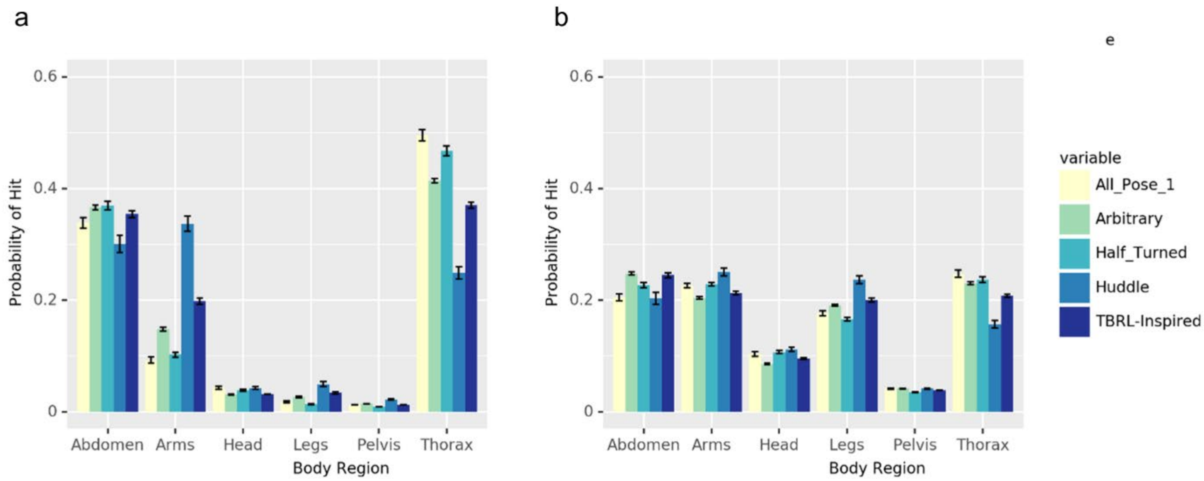

Figure 9. Relative *P*(hit) Distributions Computed for the Center-Torso Aim Point at (a) Close Range and (b) Long Range for Several Example Posture Distributions. Color corresponds to posture distribution. Error bars correspond to estimated standard error of *p*(hit) for each posture distribution and body region.

The p(hit) distribution does show some dependence on posture distribution. The "Huddle" distribution shows the highest p(hit) for the arms and legs and lowest p(hit) for the thorax. That result occurs because the "Huddle" distribution is entirely composed of subjects protecting their torsos with their arms. The "Half-Turned" and "All_Pose_1" distributions show the opposite trends (lowest p(hit) for arms and legs, highest p(hit) for thorax) at close range, but at long range the "TBRL-Inspired" and "Arbitrary" posture distributions show the lowest values for p(hit) to the arms and head and highest p(hit) to the abdomen. The "TBRL-Inspired" and "Arbitrary" distributions also show the lowest p(hit) to the head at close range because these distributions included a high proportion of "protect head" poses.

Although not shown in the figure, the belt-buckle aim point p(hit) was greatest for abdomen, legs, and pelvis at close range, with increased p(hit) for the arms, thorax, and head at long range. Also, the posture-distribution dependence of p(hit) was smaller for the belt-buckle aim point, the largest differences being seen for the "TBRL-Inspired" vs. "All Pose 1" distributions.

The next step in our analysis was to apply these p(hit) distributions to some hypothetical body-region-specific RSI distributions to determine the overall effect on RSI. Table 6 summarizes the region-based RSI distributions that we used. Each distribution lists conditional RSI values $\{RSI_b\}$ associated with impacts to the different body regions (e.g., if the arm is hit, the risk of significant injury is *X*). In a true analysis of RSI for a particular weapon, this value would be determined by aggregating the risks computed for a set of local impact locations and injury types within a body region. That process is not the focus of this report.

Table 6. Region-Specific RSI Distributions

Distribution Name	Distribution Description	Distribution Composition
Arm-Lo	Distribution with high injury risk for impacts to the torso, and low injury risk for impacts to the extremities	Arm and Leg RSI: 1% Thorax and Abdomen RSI: 10% Pelvis RSI: 5% Head RSI: 100%
Arm-Hi	Distribution with high injury risk for impacts to the arms and low injury risk for impacts to the torso	Arm RSI: 15% Leg RSI: 5% Thorax and Abdomen RSI: 1% Pelvis RSI: 5% Head RSI: 100%
All-Hi	Distribution similar to Arm-Hi, but with larger overall RSIs for each body region—representative of a weapon deployed at high-risk levels	Arm RSI: 40% Leg RSI: 20% Thorax and Abdomen RSI: 4% Pelvis RSI: 20% Head RSI: 100%

The RSI distributions in Table 6 are intended to represent different patterns of injury risk that might exist depending on the character and usage of different weapons. For example, a relatively rigid projectile may be more likely to produce fractures than soft-tissue injuries (leading to greater injury risk to the arms and legs than to the torso), while a more deformable projectile may be more likely to produce soft-tissue injuries (e.g., contusions, lacerations) than fractures (leading to greater injury risk to the torso than to the extremities). Furthermore, the same weapon deployed at a higher impact velocity can increase the RSI for all body regions. Impacts to the head are considered high risk in all cases examined here.

Figure 10 shows the outcomes for aggregate RSI as a function of pose distribution and RSI distribution. The counterintuitive outcome that longer range shots produce higher RSI is due to the spreading of the hits over a larger area encompassing higher vulnerability areas away from the aim point. We will first consider how pose distribution affects aggregate RSI relative to the "All Pose 1" distribution (representative of today's methods of estimating RSI). One encouraging result is that the "Half-Turned" distribution gives nearly identical RSI as the "All Pose 1" distribution for all conditions we considered, suggesting that ignoring the target orientation in estimating p(hit) distribution has a minimal role in determining final RSI (as long as the body-region specific RSI accounts for impact locations around the whole of each body region). Note also that simulations with ATBM of impacts of the same location from different angles *may* produce different RSI outcomes. In any assessment of particular projectiles, consideration must be made for the expected range of impact directions and conditions.

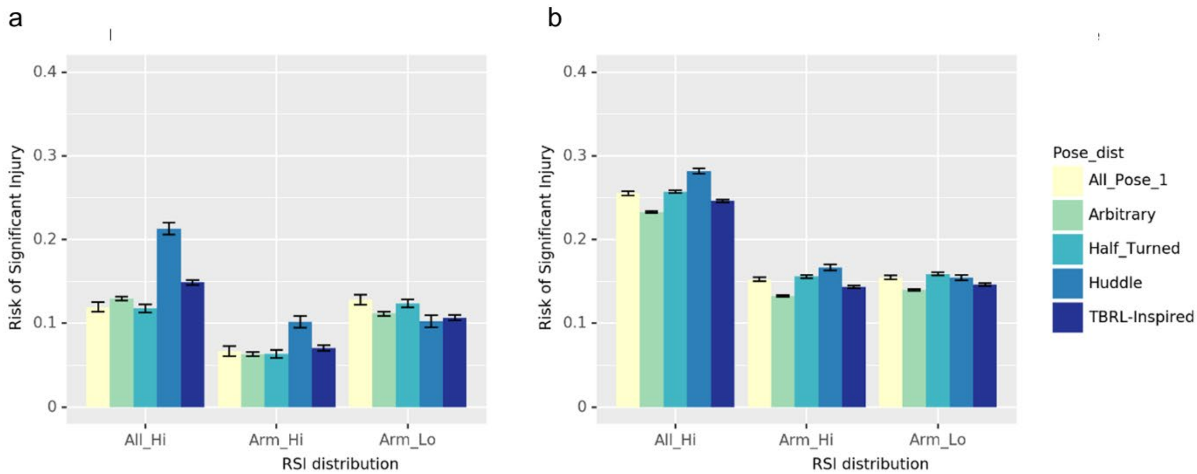

Figure 10. Aggregate Risk of Significant Injury Computed for the Center-Torso Aim Point at (a) Close Range and (b) Long Range for Several Example Posture and Body-Region Specific RSI Distributions. Color corresponds to posture distribution. Error bars correspond to estimated standard error of aggregate RSI for each posture distribution and RSI distribution.

The largest difference observed from the "All Pose 1" distribution is with the "Huddle" distribution at short range for the "All-Hi" and "Arm-Hi" cases. The "Huddle" distribution represents a situation where hits to the thorax have been traded for hits to the arms. When the arms have higher RSI than the thorax, this translates to an overall increase in RSI. When the arms have lower RSI than the thorax, the aggregate RSI decreases upon moving from "All Pose 1" to "Huddle." The other pose distributions have more subtle interactions with the aggregate RSI relative to "All Pose 1." In general, when the arms have higher risk than the thorax, defensive postures may slightly reduce aggregate RSI at long range, but at short range defensive postures can increase the RSI. When the arms have lower RSI than the torso, the RSI is reduced by defensive postures at both close and long range.

A comparison of the "Half-Turned" distribution to the "Huddle" distribution reflects the diverse ways that defensive postures affect RSI depending on the weapon's dispersion and region-specific injury-risk characteristics. At close range, the "Half-Turned" RSI is about half the "Huddle" RSI for the "All-Hi" and "Arm-Hi" RSI distributions. In contrast, the "Half-Turned" aggregate RSI is 25% higher than the "Huddle" RSI for the "Arm-Lo"

RSI distribution at close range. At long range, the RSI differences are much smaller for these two posture distributions. Therefore, we see that a crowd transitioning from a naïve state (Half-Turned) to a protective state (Huddle) could have significantly increased aggregate RSI, decreased aggregate RSI, or no change in aggregate RSI, depending on the injury-risk distribution associated with the weapon and the way it is deployed.

Meanwhile, we see that general defensive behaviors (the "Arbitrary" and "TBRL-Inspired" distributions) only reduce aggregate RSI when the RSI for the limbs is less than that for the torso and that this effect is washed out at long range when weapon dispersion spreads across most of the body.

So, while it is possible for posture distribution to have a large effect on the computed RSI (e.g., "Huddle" vs. "Half-Turned" or "All Pose 1," Close range, "All-Hi," or "Arm-Hi"), most of the cases we explored show that corrections in computed RSI due to defensive postures are small, especially considering potential uncertainties that may be introduced through estimates of RSI given a hit to a particular body region. Note, however, that this report does not cover the full range of possible distributions (RSI or postural), nor does it include the full range of weapon-dispersion characteristics. Different combinations of these inputs could produce very different aggregate RSI results. Our analysis provides a general approach for assessing aggregate RSI while accounting for the space of possible body-region specific RSI distributions, posture distributions, and weapon characteristics. We believe that this analysis can be readily tailored to reflect the particular specifications of a given operational setting and weapon CONOPs to help inform training, weapon design, and operational usage guidelines.

We also note that RSI is only one way to assess the injury risk associated with a blunt-impact projectile weapon. RSI reflects the method used by the DoD for assessing the risks associated with various IFCs, and it reflects the goal of reducing the likelihood of significant injuries of all types. It does not reflect the value judgements that individual people might have toward different types of injury. From the perspective of an individual, all "significant injuries" are not created equal. For example, a broken arm, while inconvenient, is fully reversible with appropriate medical care, but a pneumothorax or skull fracture could be fatal. Risking an arm fracture to protect the head may be preferable to risking a head injury. We do not believe our analysis should be interpreted to suggest that defensive postures are not effective at preventing serious injuries. Instead, defensive postures change which regions of the body are most likely to be hit. The analysis in this report can be used for more detailed assessments of injury risk by helping identify what kinds of behaviors increase the chance of potentially fatal injuries vs. injuries that have a high chance of recovery with appropriate medical care.

5. Conclusions

The analysis contained in this report showed that the aggregate RSI was dependent on the input weapon characteristics (body-region-specific RSI distribution, dispersion), as well as the posture distribution of the targets. Our analysis of *p*(hit) distributions found the following outcomes for specific types of defensive action for a center torso aim point:

- Crouching reduces *p*(hit) to the abdomen and thorax while increasing *p*(hit) to the arms and legs and modestly increasing *p*(hit) to the head and pelvis.
- Turning has complex interactions with *p*(hit) distribution, depending on the positions of the arms and whether the subject is also crouched.
- Protecting the head with the arms decreases *p*(hit) to the head and arms while increasing *p*(hit) to the abdomen, particularly at close range.
- Protecting the torso with the arms decreases *p*(hit) to the thorax while increasing *p*(hit) to the arms.
- Running away has a small effect on the *p*(hit) distribution at close range, but increases *p*(hit) to the abdomen and decreases *p*(hit) to the arms and head at long range.
- As weapon dispersion increases, *p*(hit) distributions spread out to cover more of the body, typically increasing relative *p*(hit) to the head, legs, and pelvis and decreasing *p*(hit) to the thorax and abdomen.

Many of these trends were consistent with the belt-buckle aim-point results, except that *p*(hit) to the legs typically decreased with range and effects on *p*(hit), while *p*(hit) to the thorax increased. Also, effects for the head, arms, and thorax were often smaller than observed for the center-torso aim point.

When these action-specific *p*(hit) distribution effects were aggregated across a mix of postures, the actual computed change in RSI caused by posture distribution relative to an "All Pose 1" distribution was only a few percentage points, in most cases. However, examples of larger changes in aggregate RSI (up to a factor of 2 in one example) were observed. Because of the breadth of variables contributing to the final value of RSI, we believe that analysis of human effects from blunt-impact projectiles is incomplete without some consideration of possible posture-dependent outcomes. Information about the probable effect of defensive postures on the risk of injury associated with use of particular weapons (especially risk *increases*) should be shared with the users of those weapons and should be considered when determining weapon CONOPs. But our results are encouraging in that they suggest that errors related to ignoring these factors in the past have probably been small relative to other uncertainties in such analysis.

This analysis does have some important limitations. First, we did not consider finer hit-position variability (e.g., the difference in risk associated with an on-rib vs. off-rib impact to the thorax). One way to account for such fine-resolution impact location variability is to base the weighting of different impact locations (and associated injury risk) in a computation of region-specific RSI on the relative cross-sectional area of different representative hit locations. For example, consider frontal impact to the head. If we estimate that the eyes and orbital sockets occupy about 20% of the cross-sectional area of the head, the RSI computed for impacts to the head should weight 20% to impacts to the eye region and 80% to impacts to the face or skull. This region-specific RSI can then be applied to an analysis like the one presented in this report for the overall computation of RSI. At the time of this writing, the sensitivity to impact location of ATBM was under active exploration.

The second major limitation of our analysis concerns our segmentation methodology. We identified potential biases in our auto-segmentation method that could be corrected with more sophisticated segmentation algorithms (perhaps including information from color images) or more accurate skeleton tracking during image collection. The most important example of this was the difficulty our algorithm exhibited distinguishing the arms from other portions of the body (see Figure 2). Protecting the torso with the arms was one of the most effective actions at changing the p(hit) distribution on the body (compare, for example, the green and blue bars in Figure 9) by trading hits to the arms and hits to other body regions. We found that this effect was probably *underestimated* by our analysis for protecting the torso, but it was probably *overestimated* for protecting the head while crouching and turned because of the biases contained in our auto-segmentation method. Improving our auto-segmentation to better distinguish the arms from the torso or head would likely affect our computed estimates of RSI differences in our notional posture distributions. Furthermore, more granular segmentation (e.g., separating the upper and lower leg or arm, segmentation of joint positions that may be high-risk RSI locations) is possible and would be beneficial for a more accurate overall RSI calculation.

Finally, our data-collection approach could have been improved by (1) recruiting our subjects from a broader pool more representative of the general population and (2) more realism in the subjects' postures. Our subjects were instructed to adopt certain defensive postures without experiencing realistic stimuli of a projectile being sent in their direction. It is possible that subjects would have behaved differently if even the appearance of such stimuli had been present. Data collected from real-world scenarios, such as photographic or video recordings of operational IFC deployments, would both inform realistic choices of posture distributions and identify whether any key behaviors were missing from our data collection.

Overall, this report has shown that defensive postures can directly affect how impacts from a blunt-impact weapon are distributed over the regions of the body. Because different regions of the body (e.g., arms, legs, head, thorax, abdomen, pelvis) can have different vulnerability to particular projectile types, changes in the distribution of impacts can affect the aggregate calculation of RSI for a particular weapon. Therefore, analysis of RSI should account for potential target responses to the IFC to inform the design, training, and CONOPs of each weapon.

Appendix A.
Additional Details on Image Acquisition and Segmentation

Silhouette Generation

To generate the silhouette image, depth thresholds were used to eliminate most of the pixels that were clearly part of the background. Then, portions of the image that were below the position of the lowest foot or to the outside of the feet and below the position of the highest foot were marked as background also. These steps were necessary because the floor near the subjects' feet would not be eliminated by the depth threshold alone. This left a region of floor between the feet still requiring elimination. Removing this region involved several steps. First, short vertical lines were marked as background at the midpoint between the feet and on the medial side of each foot to divide this section of floor from the rest of the body. Then, a flooding algorithm was used to identify the contiguous region(s) of pixels not previously marked as background that also included the center-spine joint position or one of the knee joint position. These contiguous regions were marked as body. The vertical lines drawn between the feet prevented flooding of the floor between the feet during this step. Multiple seed points were used to ensure that the whole body was captured during the flooding step, as points were sometimes mismarked in the depth image by the Kinect due to very sharp local gradients that prevented scattering of signal back toward the sensor. This could happen, for example, if a subject's arm was projected across the entire torso, producing a very sharp gradient at the edges of the arm. After the flooding step, all regions not previously marked as either background or body were then marked as background. The final result of these steps was an image with regions marked as either body or background, producing a silhouette of the subject.

Subject Brief Prior to Image Collection

This brief was read out loud to subjects before image collection, and subjects also had access to a printed copy of this brief:

> Welcome, thank you for coming.
>
> Today we are going to collect images of you doing a series of postures in front of a Kinect sensor, which collects both depth and color images.
>
> Before we start, we ask that you remove any reflective items (ID badge, watch, glasses, hair clips) and secure any loose clothing or hair. We also ask

that if you are wearing a blazer or loose sweater of any kind, that you please remove it for the photos.

We have basically three variables that we will ask you to change for the poses. First, we will manage your orientation relative to the camera. We will ask you to stand with your feet on the sticky notes that you see on the floor, either facing the camera directly (with feet on the orange and yellow sticky notes), or at a 45° angle to the camera (with feet on the orange and pink sticky notes). Second, we will ask you to either stand up straight, or crouch for the images. When crouching, we may ask you to adjust the crouch height slightly. Third, we will ask you to place your arms either at your sides (or like you are running), protecting your head, or protecting your torso. If protecting your head, please leave the center line of your face clear—this helps us with image segmentation. If protecting your torso, it is preferred to keep your arms slightly offset from the body in order to assist the depth-based image segmentation (in other words, don't squeeze). There is also one additional pose where we will ask you to face away from the camera and act as if you are running away. Please do not duck your head for that pose.

There are 13 postures, and we will ask you to go through each one twice, but we will be randomizing the order. We may occasionally ask you to repeat a pose if there is a problem with the data collection.

Because the Kinect sensor tracks movement, we may occasionally ask you to walk around or wave your arms around slowly—this is to help the sensor track you more accurately.

Do you have any questions?

Thank you for your participation!

Appendix B.
Calculations of Quantities Used in this Report

This appendix details the mathematical steps used to calculate quantities appearing in the plots in the report.

Absolute *P*(hit)

This section explains how mean absolute *P*(hit) was estimated for each pose and body region (52 images for each condition, constituting 26 subjects and 2 trials each). This section also explains how standard deviation and standard error of the mean of absolute *P*(hit) were estimated for each pose and body region. Note that these values are stored in our lookup tables for absolute *P*(hit). Also note that the mean absolute *P*(hit) for the head (which is not itself in the lookup tables) is the sum of values for skull, face, and neck. Standard deviation is based on the square root of the sum of the variances for those three body regions.

The goal of the calculations in this section is, for a given aim point and weapon dispersion, to identify the absolute probability $P(\text{hit})_{b,p}$ of hitting body segment b of a subject in pose p. We employ a Monte Carlo approach to calculate the probability by running a computational experiment in which we generate a large number of random impact locations drawn from a probability distribution representing the weapon dispersion about the aim point. With a sufficiently large number of such impact locations, this approach can be used to closely approximate integration over the underlying probability distribution.

Because the distribution of randomly selected points represents the distribution of weapon impact points around the aim point, the random set of points can remain constant over all subjects and poses. We treat the weapon-impact distribution as a bivariate normal distribution characterized by horizontal and vertical standard deviations (σ_x, σ_y) about the aim point (x_0, y_0):

$$PDF(x,y) = \frac{1}{2\pi\sigma_x\sigma_y}\exp\left(-\frac{(x-x_0)^2}{2\sigma_x^2} - \frac{(y-y_0)^2}{2\sigma_y^2}\right). \tag{B1}$$

In practice, we treat the distribution as a bivariate normal distribution in azimuth and elevation such that the absolute distribution of horizontal and vertical impact points about the aim point can be treated as the product of the range R and the angular values $\left(\theta \equiv \frac{x-x_0}{R}, \phi \equiv \frac{y-y_0}{R}\right)$,

$$PDF(\theta, \phi) = \frac{1}{2\pi\sigma_\theta\sigma_\phi} \exp\left(-\frac{\theta^2}{2\sigma_\theta^2} - \frac{\phi^2}{2\sigma_\phi^2}\right). \tag{B2}$$

Then we normalize the angles by their standard deviations $\left(\tilde{\theta} \equiv \frac{\theta}{\sigma_\theta}, \tilde{\phi} \equiv \frac{\phi}{\sigma_\phi}\right)$ to produce a bivariate standard normal distribution. In other words, we create a universal angular distribution of weapon trajectories,

$$PDF(\tilde{\theta}, \tilde{\phi}) = \exp\left(-\frac{1}{2}\left(\tilde{\theta}^2 + \tilde{\phi}^2\right)\right). \tag{B3}$$

The results of a single Monte Carlo simulation with *M* draws from the distribution in Equation (B3) are then used to represent the hit distribution for all aim points, weapons, subjects, and poses. The output of this simulation is the set of $(\tilde{\theta}_m, \tilde{\phi}_m)$ for $m = 1,2, \ldots M$. For each aim point, weapon (determining $\sigma_\theta, \sigma_\phi$), and range, the associated set of hit points is given by

$$x_m = \tilde{\theta}_m \sigma_\theta R + x_0, \; y_m = \tilde{\phi}_m \sigma_\phi R + y_0. \tag{B4}$$

For each physical experiment conducted with a subject assuming a pose and our algorithm computing a scaled and segmented body profile, the probability of a hit in segment *b* for subject *s*, pose *p*, and instance *k* is estimated as

$$\hat{P}(\text{hit})_{b,p,s,k} = \frac{1}{M} \sum_m H_{b,p,s,k}(x_m, y_m) \tag{B5}$$

where the hat (^) indicates an experimentally derived estimate, and $H_{b,p,s,k}(x_m, y_m)$ is a binary function taking the value 1 if the point (x_m, y_m) is located in body segment *b* for subject *s*, pose *p*, and instance *k* and 0 otherwise.

We assume that there is subject-to-subject variation in the posture of a given pose and that, even for a single subject, there is instance-to-instance variation. For an unbiased estimation of $P(\text{hit})_{b,p}$, we take the mean over *S* subjects and *K* instances of each pose per subject from Equation (B5),

$$\hat{P}(\text{hit})_{b,p} = \frac{1}{SK} \sum_s \sum_k \hat{P}(\text{hit})_{b,p,s,k}. \tag{B6}$$

Equation (B6) represents the best estimate of the absolute probability of a hit to given body segment for a given pose. In the body of this report, we use the normalized version of Equation (B6), the relative probability of hit as our principal metric; this will be discussed in more detail below.

We are also interested in the variance of $\hat{P}(\text{hit})_{b,p}$ (square of standard error of the mean), which will be divided into a variance due to intra-subject variation and a variance due to inter-subject variation. In general, the intra-subject variation may not be independent of subject. In other words, some subjects will consistently adopt postures, and others will exhibit high variability of a pose from instance to instance. Nevertheless, we are interested in the overall population variance as estimated from the subject-to-subject and intra-subject variation observed in our experiments.

Let the true probability $P(\text{hit})_{b,p,s,k}$ be treated as a population mean plus random contributions stemming from the choice of subject (*f*) and the particular instance (*g*),

$$P(\text{hit})_{b,p,s,k} = P(\text{hit})_{b,p} + f_{b,p,s} + g_{b,p,s,k}. \tag{B7}$$

The subject and instance contributions *f* and *g* are zero-mean random variables uncorrelated from subject to subject for *f* and *g* and instance to instance for *g*, so

$$\langle f_{b,p,s} \rangle = 0, \tag{B8}$$

$$\langle g_{b,p,s,k} \rangle = 0, \tag{B9}$$

$$\langle f_{b,p,s} g_{b,p,s,k} \rangle = 0. \tag{B10}$$

where angle brackets $\langle\ \rangle$ indicate expectation taken as a random instance and random choice of subject over the population. Let the variances of these functions be defined as

$$\langle f_{b,p,s}^2 \rangle = \sigma_{s\ b,p}^2\ , \langle f_{b,p,s} f_{b,p,s'} \rangle = 0 \text{ for } s \neq s', \tag{B11}$$

$$\langle g_{b,p,s,k}^2 \rangle = \sigma_{k\ b,p}^2, \text{ and } \langle g_{b,p,s,k} g_{b,p,s',k'} \rangle = 0 \text{ for } (s,k) \neq (s',k'). \tag{B12}$$

Note that $P(\text{hit})_{b,p} = \langle P(\text{hit})_{b,p,s,k} \rangle$.

The variance of $P(\text{hit})_{b,p}$ across the population is defined as

$$\sigma^2(\text{hit})_{b,p} = \langle \left[P(\text{hit})_{b,p,s,k} - P(\text{hit})_{b,p} \right]^2 \rangle. \tag{B13}$$

Substituting Equation (B6) into (B13) using Equations (B8)–(B12) yields

$$\sigma^2(\text{hit})_{b,p} = \sigma_{s\ b,p}^2 + \sigma_{k\ b,p}^2. \tag{B14}$$

Until this point, we have dealt exclusively with experimental inability to perfectly estimate the population due to variation in the population and limited sampling. Now we add in a component of experimental error due to imperfect measurement. Let us define the error in $\hat{P}(\text{hit})_{b,p,s,k}$ arising from body-segmentation error and Monte Carlo approximation error (of which, we presume segmentation error dominates) as

$$\hat{P}(\text{hit})_{b,p,s,k} - P(\text{hit})_{b,p,s,k} = \epsilon'_{b,p,s,k} + \bar{\epsilon}_{b,p}, \tag{B15}$$

where we have assumed as an approximation that these errors have an unbiased component $(\epsilon'_{b,p,s,k})$ as well as a pose- and body-segment-specific non-random bias $(\bar{\epsilon}_{b,p})$ as suggested by the data in Figure 2. We assume $\epsilon'_{b,p,s,k}$ is uncorrelated between subjects and instances and that its variance and the bias captured by $\bar{\epsilon}_{b,p}$ are defined by the comparison of results using hand-segmented images and corresponding auto-segmented images. Thus,

$$\langle {\epsilon'_{b,p,s,k}}^2 \rangle = \sigma^2_{\epsilon\ b,p}, \text{ and } \langle \epsilon'_{b,p,s,k} \epsilon'_{b,p,s',k'} \rangle = 0 \text{ for } (s,k) \neq (s',k'). \tag{B16}$$

We also assume the segmentation errors are uncorrelated with f and g. From Equations (B6) and (B15),

$$\hat{P}(\text{hit})_{b,p,s,k} = P(\text{hit})_{b,p} + f_{b,p,s} + g_{b,p,s,k} + \epsilon'_{b,p,s,k} + \bar{\epsilon}_{b,p}. \tag{B17}$$

From Equations (B6) and (B17),

$$\hat{P}(\text{hit})_{b,p} = P(\text{hit})_{b,p} + \frac{1}{S}\sum_s f_{b,p,s} + \frac{1}{SK}\sum_s \sum_k \left(g_{b,p,s,k} + \epsilon'_{b,p,s,k} + \bar{\epsilon}_{b,p}\right). \tag{B18}$$

The variance in the estimate $\hat{P}(\text{hit})_{b,p}$ is given by using Equation (B18) in the definition of variance:

$$\langle \left[\hat{P}(\text{hit})_{b,p} - \langle \hat{P}(\text{hit})_{b,p} \rangle\right]^2 \rangle = \frac{\sigma^2_{S\ b,p}}{S} + \frac{\sigma^2_{K\ b,p} + \sigma^2_{\epsilon\ b,p}}{SK}. \tag{B19}$$

Both Equation (B13) and Equation (B19) are expressed in terms of the size of subject-to-subject and instance-to-instance variances. To estimate subject and instance variances, we first employ the following candidate formulation:

$$\hat{\sigma}^2_{S\ b,p} = \frac{1}{S-1}\sum_s \left[\frac{1}{K}\sum_k \hat{P}(\text{hit})_{b,p,s,k} - \hat{P}(\text{hit})_{b,p}\right]^2. \tag{B20}$$

Equation (B19) is motivated by the classical formula for estimating variance utilizing the average across all trials of the same pose and subject as the estimate for the subject-specific contribution $f_{b,p,s}$. Taking the expected value of Equation (B19) and using Equations (B16) and Equation (B17) yields

$$\langle \hat{\sigma}^2_{S\ b,p} \rangle = \sigma^2_{S\ b,p} + \frac{1}{K}\left(\sigma^2_{K\ b,p} + \sigma^2_{\epsilon\ b,p}\right), \tag{B21}$$

which shows that Equation (B20) overestimates the subject-to-subject variance because it still incorporates some within-subject variance, although reduced by a factor of K. With an estimate of the within-subject variance, we can improve upon Equation (B21). To that end, we utilize the following estimate for the within-subject variance,

$$\hat{\sigma}^2_{k\;b,p} = \frac{1}{S}\sum_s \frac{1}{K-1}\sum_{k'}\left[\hat{P}(\text{hit})_{b,p,s,k'} - \frac{1}{K}\sum_k \hat{P}(\text{hit})_{b,p,s,k}\right]^2, \tag{B22}$$

which is an average over all subjects of the estimated within-subject variance subject by subject. Utilizing Equation (B16), taking the expected value of Equation (B22), yields

$$\langle \hat{\sigma}^2_{k\;b,p} \rangle = \sigma^2_{k\;b,p} + \sigma^2_{\epsilon\;b,p}, \tag{B23}$$

showing that Equation (B22) overestimates the within-subject variance and instead provides an unbiased estimate of the within-subject measured variance folding in both the within-subject instance-to-instance variance and the experimental variance associated with poor segmentation.

Inspection of Equations (B21) and (B23) points the way to an unbiased estimate of subject-to-subject variance. To wit, augmenting Equation (B19) with a corrective multiple of Equation (B21) leads to

$$\hat{\sigma}^2_{S\;b,p} = \frac{1}{S-1}\sum_s \left[\frac{1}{K}\sum_k \hat{P}(\text{hit})_{b,p,s,k} - \hat{P}(\text{hit})_{b,p}\right]^2 - \frac{1}{KS}\sum_s \frac{1}{K-1}\sum_{k'}\left[\hat{P}(\text{hit})_{b,p,s,k'} - \frac{1}{K}\sum_k \hat{P}(\text{hit})_{b,p,s,k}\right]^2, \tag{B24}$$

with

$$\langle \hat{\sigma}^2_{S\;b,p} \rangle = \sigma^2_{S\;b,p} \tag{B25}$$

the desired unbiased estimate of subject-to-subject variance. For convenient computation, it may be useful to express Equation (B24) in terms of sums and sums of squares of measured quantities as

$$\hat{\sigma}^2_{S\;b,p} = \frac{1}{K^2}\left(\frac{KS-1}{(S-1)(K-1)S}\right)\sum_s\left[\sum_k \hat{P}(\text{hit})_{b,p,s,k}\right]^2 - \frac{1}{S-1}\frac{1}{SK^2}\left[\sum_s\sum_k \hat{P}(\text{hit})_{b,p,s,k}\right]^2 - \frac{1}{K(K-1)}\frac{1}{S}\sum_s\sum_\mathrm{k} \hat{P}(\text{hit})^2_{b,p,s,\mathrm{k}}. \tag{B26}$$

Next, we wish to estimate the errors in our experimentally derived approximations as well as our estimate of population variance. To approximate the error in our experimentally derived estimate of absolute *P*(hit), we approximate the true variances in Equation (B19) using Equations (B22)–(B26):

$$\langle\left[\hat{P}(\text{hit})_{b,p} - P(hit)_{b,p}\right]^2\rangle = \frac{1}{S^2K^2(S-1)}\left\{\mathrm{S}\sum_s\left[\sum_k \hat{P}(\text{hit})_{b,p,s,k}\right]^2 - \left[\sum_s\sum_k \hat{P}(\text{hit})_{b,p,s,k}\right]^2\right\} + \bar{\epsilon}^2_{b,p}. \tag{B27}$$

The population variance is given by Equation (B14) using the approximations in Equations (B22)–(B26):

$$\hat{\sigma}^2(\text{hit})_{b,p} = \frac{1}{S(S-1)K^2}\sum_s\left[\sum_k \hat{P}(\text{hit})_{b,p,s,k}\right]^2 - \frac{1}{S(S-1)K^2}\left[\sum_s\sum_k \hat{P}(\text{hit})_{b,p,s,k}\right]^2 + \frac{1}{SK}\sum_s\sum_k \hat{P}(\text{hit})^2_{b,p,s,k} - \sigma^2_{\epsilon\ b,p}. \tag{B28}$$

The biggest problem with these approximations is the assumption that segmentation error is uncorrelated between trials. There may be uncaptured subject-specific biases, so $\langle\epsilon'_{b,p,s,k}\epsilon'_{b,p,s,k'}\rangle$ may be nonzero.

Relative *p*(hit)

This section explains how absolute *P*(hit) and associated standard deviation (for each pose and body region) is converted to relative *p*(hit) and associated standard deviation. Relative *p*(hit) is the metric shown in Figure 3–Figure 8 in the main body of this paper. In this appendix, we adopt the notation that lower case $p(\text{hit})$ refers to relative probability and upper case $P(\text{hit})$ refers to absolute probability. The standard usage doctrine presumes that a target is fired upon until hit. Thus, every target is hit eventually, and the distribution of hit locations among body segments b for pose *p*, $p(\text{hit})_{b,p}$ is a uniformly weighted average over the population. In a different shot doctrine, the average would be weighted by the probability of each subject being hit. Here, we have assumed that a target will not switch poses during the course of firing. This is likely to be untrue, since a subject in a neutral posture may switch to a defensive posture once shots are fired. Likewise, any subject may switch to a running-away posture once shots are fired.

Relative $p(\text{hit})_{b,p,s}$ is a conditional probability, the probability that target *s* in pose *p* will be hit in segment b given a hit somewhere on the body. In accordance with Bayes' theorem,

$$p(\text{hit})_{b,p,s} = \frac{P(hit)_{b,p,s}}{\sum_{b'} P(hit)_{b',p,s}}, \tag{B29}$$

where the denominator is the total absolute *P*(hit) for subject *s*, pose *p*, determined as the sum of absolute *P*(hit) across the eight body segments. Since poses are dynamic, we assume that each shot will effectively be a new instance of each pose. In general, it may be the case that the absolute probability of hit for an instance of a pose may be correlated with the body-segment distribution for that instance. For example, posing in a deeper crouch may both reduce absolute *P*(hit) and increase the relative probability of hitting the legs. The numerator and denominator in Equation (B29) are each averages over all possible instances of the pose by the subject. Therefore, to estimate Equation (B29), we should separately estimate the numerator and denominator, each as the mean over instances for a subject and pose. Canceling out a factor of 1/*K* in both the numerator and denominator leads to

$$\hat{p}(\text{hit})_{b,p,s} = \frac{\sum_k \hat{P}(\text{hit})_{b,p,s,k}}{\sum_{k'}\sum_{b'}\hat{P}(\text{hit})_{b',p,s,k'}}. \tag{B30}$$

If we were to instead take the mean over the quotients, that would give too much weight to instances with low total absolute probability of hit (low denominator). While it is not formally true that $\langle \hat{p}(\text{hit})_{b,p,s} \rangle = p(\text{hit})_{b,p,s}$, it is true in the limit $K \to \infty$.

[15] As long as the fractional variation[16] in the denominator, which is related to the fractional instance-to-instance variation in total absolute *P*(hit), remains small, the fractional deviation of $\langle \hat{p}(\text{hit})_{b,p,s} \rangle$ from $p(\text{hit})_{b,p,s}$ should also remain small. We also note that segmentation error will not contribute to the denominator except insofar as the subjects' feet cannot be distinguished from the floor. Other segmentation errors misallocate locations to one body segment at the expense of another, so the errors will cancel out in the summation over segments.

To estimate the relative probability across the population, we take the mean across subjects of Equation (B30),

$$\hat{p}(\text{hit})_{b,p} = \frac{1}{S} \sum_s \hat{p}(\text{hit})_{b,p,s} = \frac{1}{S} \sum_s \frac{\sum_k \hat{P}(\text{hit})_{b,p,s,k}}{\sum_{k'} \sum_{b'} \hat{P}(\text{hit})_{b',p,s,k'}}. \tag{B31}$$

Because the subject-by-subject estimates are not expected to be completely unbiased, as discussed in the previous paragraph, it is also not formally true that $\langle \hat{p}(\text{hit})_{b,p} \rangle = p(\text{hit})_{b,p}$. However, the relationship in Equation (B31) does not add additional bias because over choices of ensembles of subjects,

$$p(\text{hit})_{b,p} = \langle p(\text{hit})_{b,p,s} \rangle = \langle \frac{1}{S} \sum_s p(\text{hit})_{b,p,s} \rangle, \tag{B32}$$

and neither additive nor fractional bias in the summand of (B30) would be amplified or attenuated by taking the mean over the subject samples.

Because Equation (B29) is a quotient of random variables, there is no straightforward analytical relationship between the variances of the absolute *P*(hit) contributions from the previous section and the variances for relative *p*(hit). Therefore, some additional assumptions or simplifications are necessary to establish the variances for relative *p*(hit).

One speculative approach is to mimic Equation (B17) and start fresh with a linear model for the variability of the measurements of relative *p*(hit). For this approach, let us assume that

$$\hat{p}(\text{hit})_{b,p,s} = p(\text{hit})_{b,p,s} + \bar{G}_{b,p} + G'_{b,p,s}, \tag{B33}$$

[15] Note that the experiments described here with $K = 2$ are very far from the asymptote.

[16] Fractional variation refers to errors of, for instance, ±10% rather than ± some fixed amount.

where $\bar{G}_{b,p}$ is a non-stochastic measurement bias associated with a pose and body segment, and $G'_{b,p,s}$ is a zero-mean random measurement error uncorrelated from subject to subject, such that

$$\langle G'_{b,p,s}\rangle = 0, \langle G'_{b,p,s}G'_{b,p,s'}\rangle = 0 \text{ for } s \neq s', \text{and } \langle {G'_{b,p,s}}^2\rangle = \sigma^2_{G\,b,p}. \tag{B34}$$

Note that Equation (B32) is an ad hoc assumption inconsistent with Equations (B6) and (B17); however, without a simplification such as Equation (B33), we are not able to derive a closed-form estimate for the variance in the estimate of relative *p*(hit) due to the nonlinearity of Equation (B29). Equation (B33) effectively treats $\hat{p}(\text{hit})_{b,p,s}$ as the fundamental measured quantity:

$$\langle\hat{p}(\text{hit})_{b,p,s}\rangle_k = p(\text{hit})_{b,p,s} + \bar{G}_{b,p}, \tag{B35}$$

where the expectation in Equation (B35) is only over instances as indicated by the subscript *k*, not over subjects. Taking the expectation over subjects results in

$$\langle\hat{p}(\text{hit})_{b,p,s}\rangle = p(\text{hit})_{b,p} + \bar{G}_{b,p}, \tag{B36}$$

and from Equations (B30) and (B35),

$$\langle\hat{p}(\text{hit})_{b,p}\rangle = p(\text{hit})_{b,p} + \bar{G}_{b,p}. \tag{B37}$$

Next, we examine the variance in the estimate.

$$\left\langle\left(\hat{p}(\text{hit})_{b,p} - \langle\hat{p}(\text{hit})_{b,p}\rangle\right)^2\right\rangle = \frac{1}{S^2}\sum_s\sum_{s'}\langle p(\text{hit})_{b,p,s}p(\text{hit})_{b,p,s'}\rangle - p(\text{hit})^2_{b,p} + \frac{1}{S}\sigma^2_{G\,b,p}. \tag{B38}$$

To resolve the first term on the right-hand-side of Equation (B38), we further assume that the relative *p*(hit) for each subject consists of a subject-independent contribution and a random subject-specific contribution,

$$p(\text{hit})_{b,p,s} = p(\text{hit})_{b,p} + F_{b,p,s}, \tag{B39}$$

with

$$\langle F_{b,p,s}\rangle = 0, \langle F_{b,p,s}F_{b,p,s'}\rangle = 0 \text{ for } s \neq s', \text{and } \langle {F_{b,p,s}}^2\rangle = \sigma^2_{F\,b,p} \tag{B40}$$

When we compare Equations (B33), (B34), (B39), and (B40), it is apparent that the contributions of $F_{b,p,s}$ and $G'_{b,p,s}$ cannot be distinguished. As would be expected then, incorporating Equations (B39) and (B40) into (B38) yields

$$\left\langle\left(\hat{p}(\text{hit})_{b,p} - \langle\hat{p}(\text{hit})_{b,p}\rangle\right)^2\right\rangle = \frac{1}{S}\left(\sigma^2_{F\,b,p} + \sigma^2_{G\,b,p}\right). \tag{B41}$$

Equation (B41) is the expected square of the estimation error (exclusive of the bias) in $\hat{p}(\text{hit})_{b,p}$.

Also of interest is the subject-to-subject population variance in relative p(hit),

$$\langle\left(p(\text{hit})_{b,p,s} - p(\text{hit})_{b,p}\right)^2\rangle = \sigma_F^2{}_{b,p}. \tag{B42}$$

To estimate Equations (B41) and (B42), we need estimates for the variances and bias:

$$\hat{\sigma}_F^2{}_{b,p} + \hat{\sigma}_G^2{}_{b,p} = \frac{1}{S-1}\sum_s\left[\hat{p}(\text{hit})_{b,p,s} - \hat{p}(\text{hit})_{b,p}\right]^2, \tag{B43}$$

$$\langle\hat{\sigma}_F^2{}_{b,p} + \hat{\sigma}_G^2{}_{b,p}\rangle = \sigma_F^2{}_{b,p} + \sigma_G^2{}_{b,p}. \tag{B44}$$

Unfortunately, there is no way in this model to disentangle $\sigma_F^2{}_{b,p}$ and $\sigma_G^2{}_{b,p}$, so there is not enough information here to estimate population variance.

An alternate approach, which we employed to compute the results shown in the main body of this paper, is to replace the approximation in Equation (B30) with its close relation,

$$\hat{p}(\text{hit})_{b,p,s} = \frac{1}{K}\sum_k \frac{\hat{P}(\text{hit})_{b,p,s,k}}{\sum_{b'}\hat{P}(\text{hit})_{b',p,s,k}}, \tag{B45}$$

which effectively treats the total absolute probability of a hit as varying little from instance to instance within each subject. In this approach, the summand of Equation (B45) becomes the fundamental measurement variable with

$$\hat{p}(\text{hit})_{b,p,s,k} = \frac{\hat{P}(\text{hit})_{b,p,s,k}}{\sum_{b'}\hat{P}(\text{hit})_{b',p,s,k}}. \tag{B46}$$

Using Equation (B46) as a starting point, the entire absolute P(hit) analysis can be utilized, leading to estimates of relative p(hit) analogous to Equation (B5):

$$\hat{p}(\text{hit})_{b,p} = \frac{1}{SK}\sum_s\sum_k \hat{p}(\text{hit})_{b,p,s,k}, \tag{B47}$$

with

$$\langle\hat{p}(\text{hit})_{b,p}\rangle = p(\text{hit})_{b,p} + \tilde{\tilde{\epsilon}}_{b,p}, \tag{B48}$$

the estimation variance analogous to Equation (B27):

$$\langle\left[\hat{p}(\text{hit})_{b,p} - \langle\hat{p}(\text{hit})_{b,p}\rangle\right]^2\rangle = \frac{1}{S^2K^2(S-1)}\left\{S\sum_s\left[\sum_k\hat{p}(\text{hit})_{b,p,s,k}\right]^2 - \left[\sum_s\sum_k\hat{p}(\text{hit})_{b,p,s,k}\right]^2\right\}, \tag{B49}$$

and population variance analogous to Equation (B28):

$$\tilde{\hat{\sigma}}^2(\text{hit})_{b,p} = \frac{1}{S(S-1)K^2}\sum_s\left[\sum_k \hat{p}(\text{hit})_{b,p,s,k}\right]^2 - \frac{1}{S(S-1)K^2}\left[\sum_s\sum_k \hat{p}(\text{hit})_{b,p,s,k}\right]^2 + \frac{1}{SK}\sum_s\sum_k \hat{p}(\text{hit})^2_{b,p,s,k} - \tilde{\sigma}^2_{\epsilon\ b,p}, \tag{B50}$$

where the tilde (~) over the variance and bias indicates the relative p(hit) quantity corresponding to the absolute P(hit) quantity without the tilde.

Equation (B47) is the basis for the principal values plotted in Figure 3–Figure 8, while the error bars in panels a and b of Figure 3 and Figure 5–Figure 8 and panel a of Figure 4 are the square root of Equation (B49).[17] For the difference plots (panels c and d) in Figure 3 and Figure 5–Figure 8 and panel b in Figure 4, the error bars are the square root of the sum of the two contributing variances from Equation (B49). As further clarification, Equation (B49) computes variance in the estimate of the mean $p(\text{hit})_{b,p}$ (analogous to a standard error of the mean), while Equation (B50) computes the population variance of $p(\text{hit})_{b,p}$. This latter variance is a description of variation in the population, rather than an estimate of uncertainty.

Analysis of Segmentation Error

This section explains how the manual- vs. automatic-segmentation errors were estimated.

The automatic-segmentation algorithm can systematically fail to properly separate body segments in various poses. For example, arms and torso can be difficult to accurately separate when the arms are in front of and close to the torso. To capture these and other segmentation errors, we manually segmented two images per pose, each from a different subject. This dataset is sparser than would be desired for a full characterization of the segmentation error, but collection of a more complete dataset would have been too labor intensive for this effort. Nevertheless, the data were sufficient to observe some level of bias and variance as well as trends consistent across poses, as discussed in the main body of this report.

Treating the manual segmentation as truth and neglecting Monte Carlo sampling errors, we use the corresponding manual- and automatic-segmentation errors to generate $p(\text{hit})_{b,p,s,k}$ and $\hat{p}(\text{hit})_{b,p,s,k}$ respectively. Note that the manual-segmentation result is granted the "truth" notation utilized in this appendix. The discrepancy is given by

$$\hat{p}(\text{hit})_{b,p,s,k} - p(\text{hit})_{b,p,s,k} = \tilde{\epsilon}'_{b,p,s,k} + \tilde{\bar{\epsilon}}_{b,p}. \tag{B51}$$

[17] For the head, the error bars shown in panels a and b are the square root of the sum of the contributing estimation variances from the face, neck, and skull body regions computed with Equation (B49).

For these data, for each p, only one k is available for each of two values of s. We refer to the cardinality of the limited set for each pose as $S^* = 2$. For estimating the bias, we note that

$$\tilde{\bar{\epsilon}}_{b,p} = \langle \tfrac{1}{S^*} \sum_s \big(\hat{p}(\text{hit})_{b,p,s,k} - p(\text{hit})_{b,p,s,k}\big) \rangle, \tag{B52}$$

so an unbiased estimate of the bias is given by

$$\hat{\tilde{\bar{\epsilon}}}_{b,p} = \tfrac{1}{S^*} \sum_s \big(\hat{p}(\text{hit})_{b,p,s,k} - p(\text{hit})_{b,p,s,k}\big). \tag{B53}$$

For the random portion of the error,

$$\langle \tfrac{1}{S^*} \sum_s \big(\hat{p}(\text{hit})_{b,p,s,k} - p(\text{hit})_{b,p,s,k}\big)^2 \rangle = \tilde{\sigma}^2_{\epsilon\ b,p} + \tilde{\bar{\epsilon}}^2_{b,p}, \tag{B54}$$

where we note that the prefactor is the reciprocal of S^* rather than $(S^* - 1)$ because the ground-truth is used as the reference rather than the experimentally derived estimate of the mean. Thus, the estimate of the random segmentation error is given by

$$\hat{\tilde{\sigma}}^2_{\epsilon\ b,p} = \tfrac{1}{S^*} \sum_s \big(\hat{p}(\text{hit})_{b,p,s,k} - p(\text{hit})_{b,p,s,k}\big)^2 - \left[\tfrac{1}{S^*} \sum_s \big(\hat{p}(\text{hit})_{b,p,s,k} - p(\text{hit})_{b,p,s,k}\big)\right]^2 \tag{B55}$$

We acknowledge the coarse nature of these estimates based on merely two data points. In fact, the variance of these estimates is given by

$$\langle \big(\hat{\tilde{\bar{\epsilon}}}_{b,p} - \tilde{\bar{\epsilon}}_{b,p}\big)^2 \rangle = \tfrac{1}{S^*} \tilde{\sigma}^2_{\epsilon\ b,p}, \tag{B56}$$

and

$$\langle \big(\hat{\tilde{\sigma}}^2_{\epsilon\ b,p} - \tilde{\sigma}^2_{\epsilon\ b,p}\big)^2 \rangle = \left(-\tfrac{1}{S^*} + \tfrac{5}{S^{*2}} - \tfrac{3}{S^{*3}}\right) \tilde{\sigma}^4_{\epsilon\ b,p} + \left(\tfrac{1}{S^*} - \tfrac{2}{S^{*2}} + \tfrac{1}{S^{*3}}\right) \langle \tilde{\epsilon}'^{\,4}_{b,p,s,k} \rangle. \tag{B57}$$

For random errors conforming to a normal distribution, Equation (B57) reduces to

$$\langle \big(\hat{\tilde{\sigma}}^2_{\epsilon\ b,p} - \tilde{\sigma}^2_{\epsilon\ b,p}\big)^2 \rangle = \left(2 - \tfrac{1}{S^*}\right) \tfrac{1}{S^*}\ \tilde{\sigma}^4_{\epsilon\ b,p}. \tag{B58}$$

For $S^* = 2$, the value in our sample, the standard deviation of the estimate for the variance from Equation (B58) is about 87% of the estimated value. In other words, the error bars in the estimate of $\tilde{\sigma}_{\epsilon_{b,p}}$ are nearly as large as $\tilde{\sigma}_{\epsilon_{b,p}}$ itself. But, especially if the bias $\tilde{\bar{\epsilon}}_{b,p}$ is large compared with the random error $\tilde{\sigma}_{\epsilon_{b,p}}$, estimates of the bias using Equation (B56) will have small error bars relative to the size of the bias itself.

Looking back at Equations (B47)–(B50), we can now examine how the segmentation errors affect our p(hit) estimates. Equation (B53) gives the approximate bias in Equation (B47), the estimate of $p(\text{hit})_{b,p}$. Equation (B53) is plotted in the colored bars in Figure 2. Equation (B56), using the approximation in Equation (B55), gives the square of the error bars in Figure 2. Equation (B55) gives the approximate variance of the random component of the error, which is required in Equation (B50) to estimate the population variance. However, due to the large uncertainty in $\hat{\hat{\sigma}}^2_{\epsilon\,b,p}$, as demonstrated in Equation (B58), the error bars in Figure 2 and the correction in Equation (B50) are very rough. Ignoring the correction in Equation (B50) would give a conservatively high estimate of population variance.

As discussed in the main body of the paper, certain trends in the automated-segmentation bias can be observed across poses. These can be observed in some cases via direct observation of consistent segmentation effects (rather than their influence on p(hit)), such as misidentification of joint locations, as well as via aggregation of common postural components across poses (e.g., crouched poses may have a common effect on the hip joints, leading to consistent segmentation irregularities for the legs). We also have increased confidence in some of the bias trends due to their consistency across poses. For instance, looking at the bias in p(hit) for the pelvis in Figure 2, the effect is in a consistent direction for 10 or 12 out of 13 poses, depending on the weapon dispersion. A simple binomial calculation shows that the likelihood of such a skewed effect (10/13 or 12/13 trials showing bias in the same direction) appearing when no bias exists is 9% or 0.3%, respectively.[18] This suggests a high confidence that the bias effects exhibited in Figure 2 are real despite the sparse dataset.

Aggregation Across Pose Distributions

This section explains how the body region relative p(hit) and associated standard deviation is estimated for a given pose distribution. The relative p(hit) aggregated across poses $p(\text{hit})_b$ is given by a weighted average over the relative p(hit) for each pose $p(\text{hit})_{b,p}$ with the weights w_p given by the fraction of encounters in each pose p,

$$p(\text{hit})_b = \sum_p w_p p(\text{hit})_{b,p}, \tag{B59}$$

which we estimate as

[18] This calculation is done by computing the probability that at least 10 or 12 out of 13 trials show bias in the same direction when there is in fact no bias in either direction (i.e., the null hypothesis is that the chance of observing a positive bias is equal to the chance of observing a negative bias, or 50%). Using the probability mass function for Bernoulli trials, we compute $P(k \geq 10) + P(k \leq 4)$ and $P(k \geq 12) + P(k \leq 2)$, where k is the number of trials that show a positive bias.

$$\hat{p}(\text{hit})_b = \sum_p \hat{w}_p \hat{p}(\text{hit})_{b,p}, \tag{B60}$$

where, in general, the $\hat{w}_p$ will differ from the true w_p. Equation (B60) corresponds to Equation (6) in the main body of the report and is plotted in Figure 9. We assume the error $\Delta w_p = \hat{w}_p - w_p$ is unbiased and independent of any errors $\hat{p}(\text{hit})_{b,p} - p(\text{hit})_{b,p}$. Even though errors in the prevalence of one pose come at the expense of the estimated prevalence of other poses, we make the coarse approximation that the errors are independent and uniform in expected magnitude across poses,

$$\langle \Delta w_p \rangle = 0, \langle \Delta w_p^2 \rangle = \sigma_P^2, \langle \Delta w_p \Delta w_{p'} \rangle = 0 \text{ for } p \neq p'. \tag{B61}$$

This allows us to estimate the consequences of a coarse level of pose-distribution uncertainty on the aggregated *p*(hit). The sum of the weights must be one:

$$\sum_p w_p = 1, \sum_p \hat{w}_p = 1. \tag{B62}$$

Because the expectation of a product of independent variables is the product of the expectation,

$$\langle \hat{p}(\text{hit})_b \rangle = \sum_p \langle \hat{w}_p \rangle \langle \hat{p}(\text{hit})_{b,p} \rangle, \tag{B63}$$

and

$$\langle \hat{p}(\text{hit})_b \rangle = p(\text{hit})_b + \sum_p w_p \tilde{\tilde{\epsilon}}_{b,p}, \tag{B64}$$

where we have utilized Equation (B48). In other words, the bias in the pose-aggregated *p*(hit) is the weighted average of the biases in each pose-specific *p*(hit) with weighting based on true pose prevalence.

The variance in the estimate is given by

$$\langle [\hat{p}(\text{hit})_b - \langle \hat{p}(\text{hit})_b \rangle]^2 \rangle = \sigma_P^2 \sum_p \left(p(\text{hit})_{b,p} + \tilde{\tilde{\epsilon}}_{b,p} \right)^2 + \sum_p w_p^2 \left[\frac{1}{S} \sigma_{s\ b,p}^2 + \frac{1}{SK} \left(\sigma_{k\ b,p}^2 + \sigma_{\epsilon\ b,p}^2 \right) \right] + \sum_p \sigma_P^2 \left[\frac{1}{S} \sigma_{s\ b,p}^2 + \frac{1}{SK} \left(\sigma_{k\ b,p}^2 + \sigma_{\epsilon\ b,p}^2 \right) \right]. \tag{B65}$$

Equation (B65) follows a form along the following lines: if $C = AB$, then the error in C has contributions from the error in *A* times the value of *B*, the error in *B* times the value of *A*, and the product of the errors in *A* and *B*. In this case, *A* is the pose prevalence and *B* is the pose-specific $p(\text{hit})_{b,p}$, where

$$\langle \left[\hat{p}(\text{hit})_{b,p} - \langle \hat{p}(\text{hit})_{b,p} \rangle \right]^2 \rangle = \frac{1}{S} \sigma_{s\ b,p}^2 + \frac{1}{SK} \left(\sigma_{k\ b,p}^2 + \sigma_{\epsilon\ b,p}^2 \right). \tag{B66}$$

In the main body of the report, Equation (7) corresponds to the square-root of Equation (B65) when the pose distribution is certain ($\sigma_P = 0$) and is used as the basis for the error bars in Figure 9.

Equations (B65) and (7) make an assumption that the $\hat{p}(\text{hit})_{b,p}$ are uncorrelated across poses for each body part. We enumerate three ways this assumption could be flawed. This assumption could be violated if the body proportions of the subjects in the experiment deviated from the population-wide body proportions in a systematic way and to a degree substantially larger than that expected of any given random sampling of the population. For instance, this could be the case if our subject pool predominantly had substantially thinner-than-average arms such that the relative population-wide probability of hitting the arms was underestimated for all poses. However, this would produce a bias rather than an increased variance. In our analysis, we assumed that our subject pool was population-representative and neglected systematic sampling errors. The $\{\hat{p}(\text{hit})_{b,p}\}$ could also be correlated across poses due to systematic errors in automated body segmentation. As shown in Equation (B64), this effect would also produce a bias in the estimate but not an increased variance. Finally, the subject-to-subject variance could be dominated by body geometry rather than by the ways different subjects assume the different poses. If that were the case, subjects with thin arms would show lower probability of hitting the arms in all poses, and subjects with larger heads would show higher probability of hitting the head in all poses. These are the types of correlations that would cause unmodeled changes to the variance. We did not explore whether our data contain evidence of this effect. If present, these correlations would predominantly be positive correlations leading to higher variance, meaning that Equation (7) would underestimate the true standard deviation.

Aggregate RSI Calculation

This section explains how errors in p(hit) affect estimates of the aggregate RSI for a given RSI distribution and pose distribution. The RSI is given by the sum over the body parts of the product of the probability of a hit to each body part and the probability of a serious injury given a hit to that body part $P_{SI|\text{hit}_b}$:

$$RSI = \sum_b P_{SI|\text{hit}_b} p(\text{hit})_b. \tag{B67}$$

Equation (B67) follows the same $C = AB$ pattern described above. Therefore, by comparison to the previous section, for unbiased $\hat{P}_{SI|\text{hit}_b}$ with estimation variance $\sigma^2_{SI|\text{hit}_b}$,

$$\widehat{RSI} = \sum_b \hat{P}_{SI|\text{hit}_b} \hat{p}(\text{hit})_b, \tag{B68}$$

$$\langle \widehat{RSI} \rangle = RSI + \sum_b P_{SI|\text{hit}_b} \sum_p w_p \bar{\bar{\epsilon}}_{b,p}, \tag{B69}$$

$$\langle[\widehat{RSI} - \langle\widehat{RSI}\rangle]^2\rangle = \sum_b \left(P^2_{SI|\text{hit}_b} + \sigma^2_{SI|\text{hit}_b}\right)\left\{\sigma_P^2 \sum_p \left(p(\text{hit})_{b,p} + \bar{\bar{\epsilon}}_{b,p}\right)^2 + \sum_p w_p^2 \left[\frac{1}{S}\sigma^2_{s\ b,p} + \frac{1}{SK}\left(\sigma^2_{k\ b,p} + \sigma^2_{\epsilon\ b,p}\right)\right] + \sum_p \sigma_P^2 \left[\frac{1}{S}\sigma^2_{s\ b,p} + \frac{1}{SK}\left(\sigma^2_{k\ b,p} + \sigma^2_{\epsilon\ b,p}\right)\right]\right\} + \sum_b \sigma^2_{SI|\text{hit}_b}\left(p(\text{hit})_b + \sum_p w_p \bar{\bar{\epsilon}}_{b,p}\right)^2, \quad \text{(B70)}$$

where the portion of Equation (B70) in curly braces is directly taken from Equation (B65). Equation (8) in the main body of the report corresponds to Equation (B68), and Equation (9) corresponds to the square-root of Equation (B70); these are plotted as the values and error bars (for $\sigma_P = 0$ and $\sigma_{SI|\text{hit}_b} = 0$), respectively, in Figure 10. In Equation (B69), just as in (B64), the bias in the RSI estimate is the weighted sum of the biases in its contributing factors for each body part and pose. If errors are assumed to represent a small fraction of their base quantities, then the terms corresponding to the product of errors can be approximately neglected. In this approximation, Equation (B70) reduces to

$$\langle[\widehat{RSI} - \langle\widehat{RSI}\rangle]^2\rangle = \sum_b P^2_{SI|\text{hit}_b}\left\{\sigma_P^2 \sum_p \left(p(\text{hit})_{b,p} + \bar{\bar{\epsilon}}_{b,p}\right)^2 + \sum_p w_p^2 \left[\frac{1}{S}\sigma^2_{s\ b,p} + \frac{1}{SK}\left(\sigma^2_{k\ b,p} + \sigma^2_{\epsilon\ b,p}\right)\right]\right\} + \sum_b \sigma^2_{SI|\text{hit}_b}\left(p(\text{hit})_b + \sum_p w_p \bar{\bar{\epsilon}}_{b,p}\right)^2. \quad \text{(B71)}$$

As with the aggregation across poses, the estimated variance in the aggregation across body parts in Equations (9) and (B70) assumes statistical independence of the contributing quantities. In this case, the primary concern is that, because the $\hat{p}(\text{hit})_b$ sum to 1, they must be correlated. The correlation between the probability of hitting various body parts is likely to be negative because erroneously increasing the relative probability of hitting one body part must come at the expense of decreasing the relative probability of hitting another body part. Negative correlations would lead to a lower aggregated variance. Neglecting these correlations, as is done in Equations (9) and (B70), would therefore produce an overestimate of the standard deviation.

Appendix C.
Data for Belt-Buckle Aim Point

This section provides the equivalents of Figure 2, Figure 3, and Figure 5 through Figure 10 for the belt-buckle aim point.

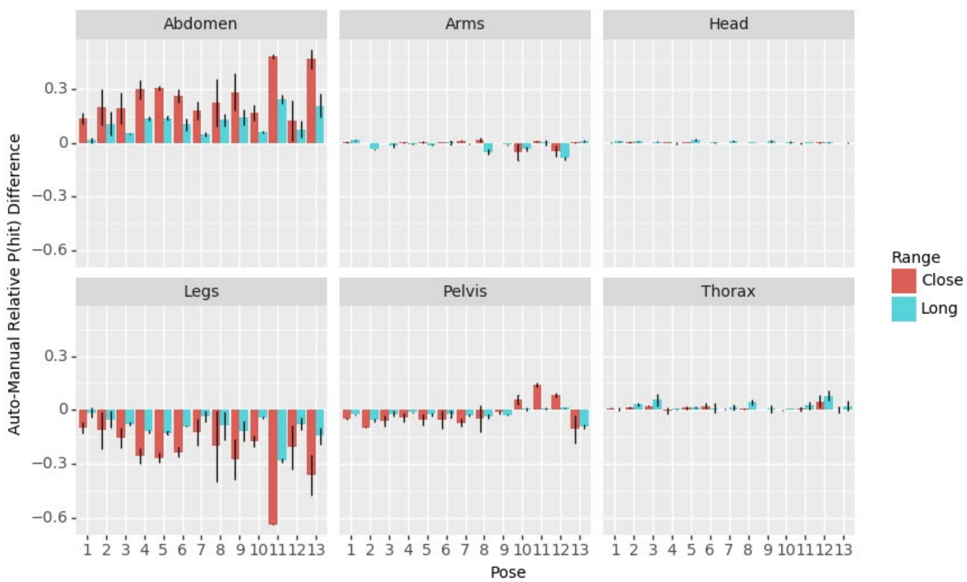

Figure C-1. Average Differences in Relative *p*(hit) between Auto-segmented and Manually Segmented Images ($\widehat{p}_{diff}$) for Belt-Buckle Aim Point. Bar color indicates close- and long-range weapon-dispersion patterns. Error bars indicate standard error of the difference computed in this way for two images.

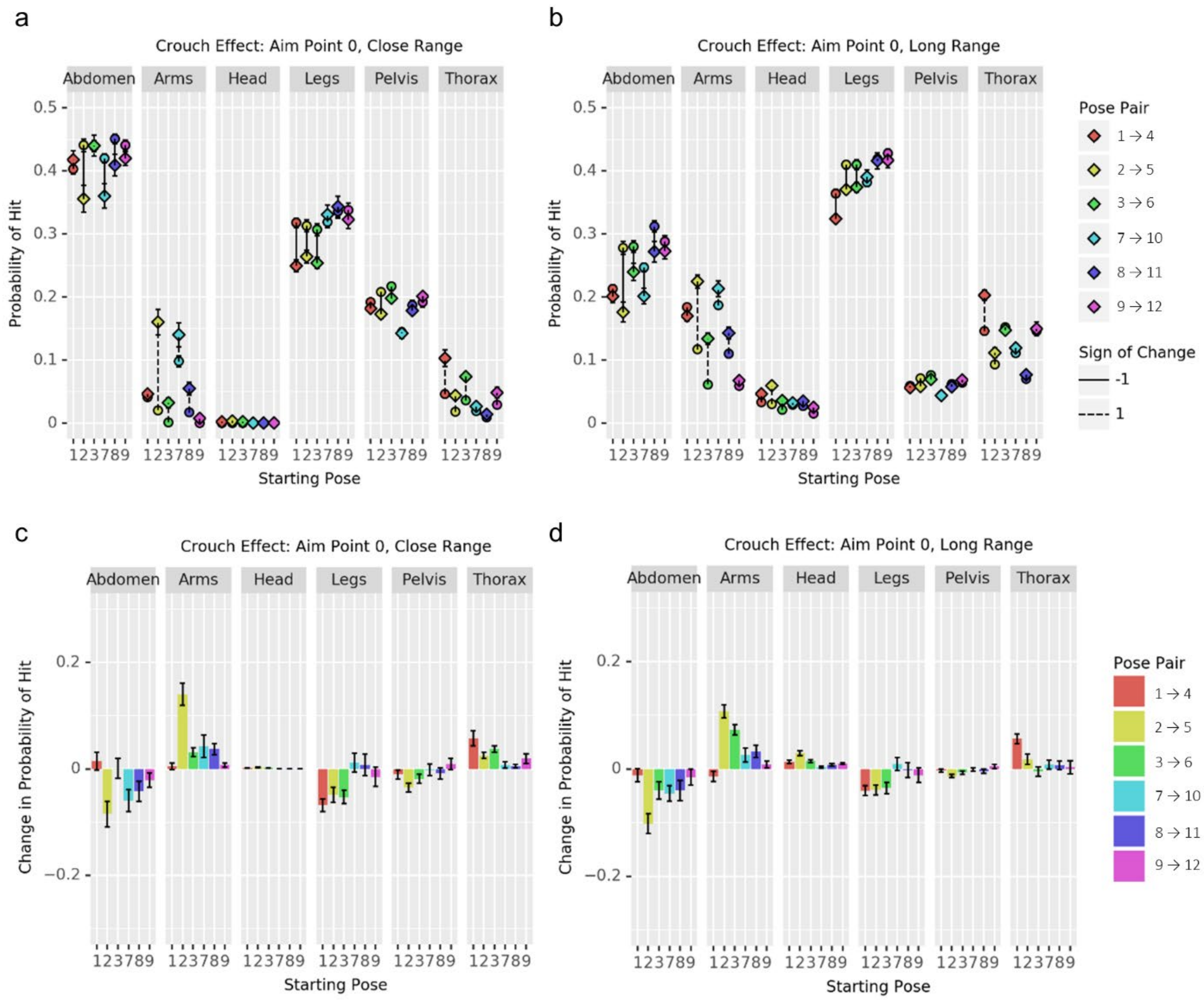

Figure C-2. Changes in Relative *p*(hit) Distribution Across Six Body Regions for Crouch Action. These plots correspond to the belt-buckle aim point (Aim Point 0), with data aggregated across 52 images for each posture and body region. Color represents the starting posture in transitions defined in Table 4. (a, b) Relative *p*(hit) before (circles) and after (diamonds) the subject crouches for (a) short-range and (b) long-range weapon dispersion. Solid lines indicate that crouching decreased *p*(hit) for that starting posture and body region. Dashed lines indicate that crouching increased *p*(hit). Error bars represent standard error of the mean for starting and ending expected *p*(hit). (c, d) Change in relative *p*(hit) for crouch posture pairs for (c) short-range and (d) long-range weapon dispersion. Error bars represent standard error of the mean for change in *p*(hit).

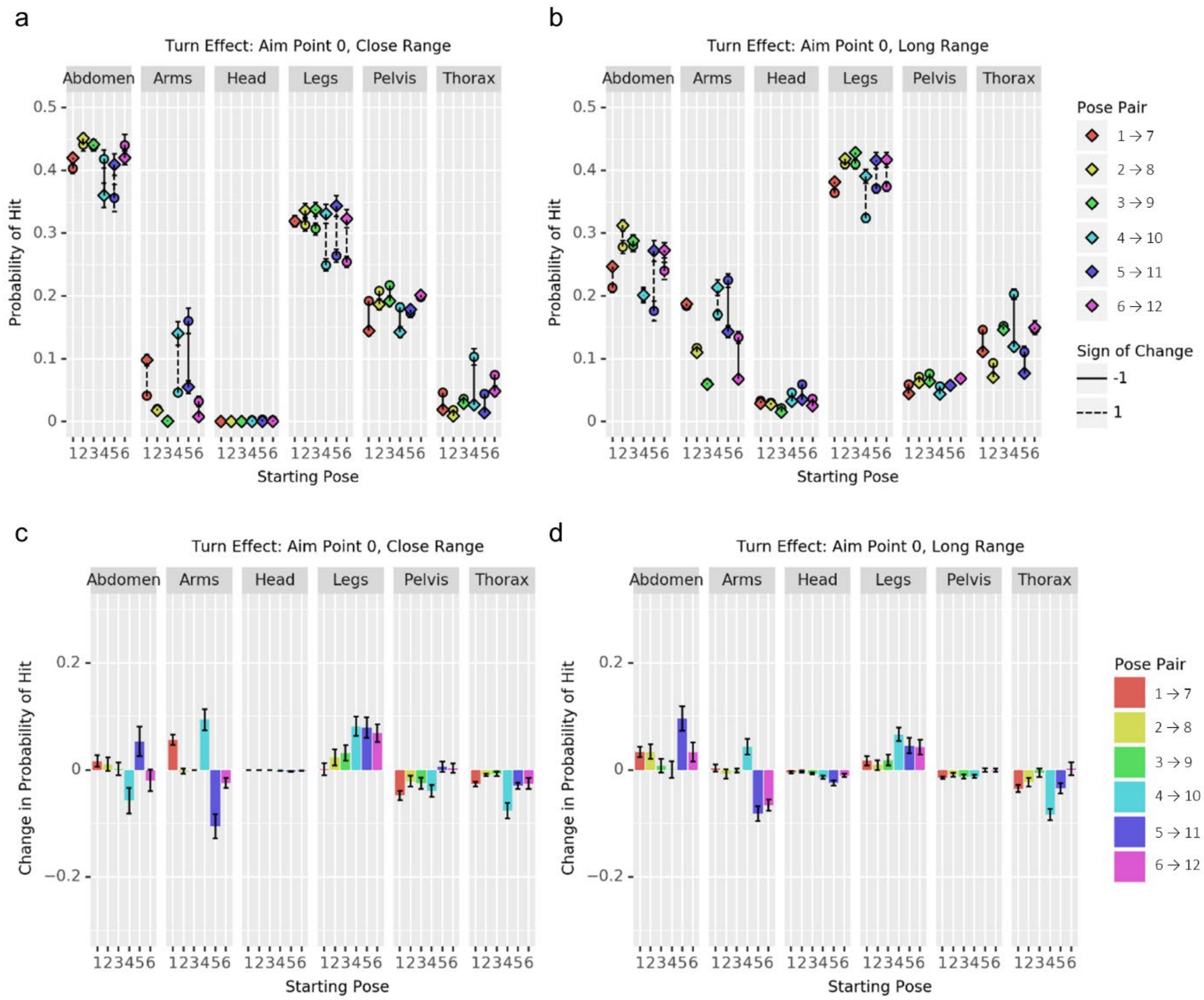

Figure C-3. Changes in Relative *p*(hit) Distribution Across Six Body Regions for Turn Action. These plots correspond to the belt-buckle aim point (Aim Point 0), with data aggregated across 52 images for each pose and body region. Color represents the starting posture in transitions defined in Table 4. (a, b) Relative *p*(hit) before (circles) and after (diamonds) the subject turns to a 45° partial profile relative to the camera for (a) short-range and (b) long-range weapon dispersion. Solid lines indicate that turning decreased *p*(hit) for that starting posture and body region. Dashed lines indicate that turning increased *p*(hit). Error bars represent standard error of the mean for starting and ending expected *p*(hit). (c, d) Change in relative *p*(hit) for turn posture pairs for (c) short-range and (d) long-range weapon dispersion. Error bars represent standard error of the mean for change in *p*(hit).

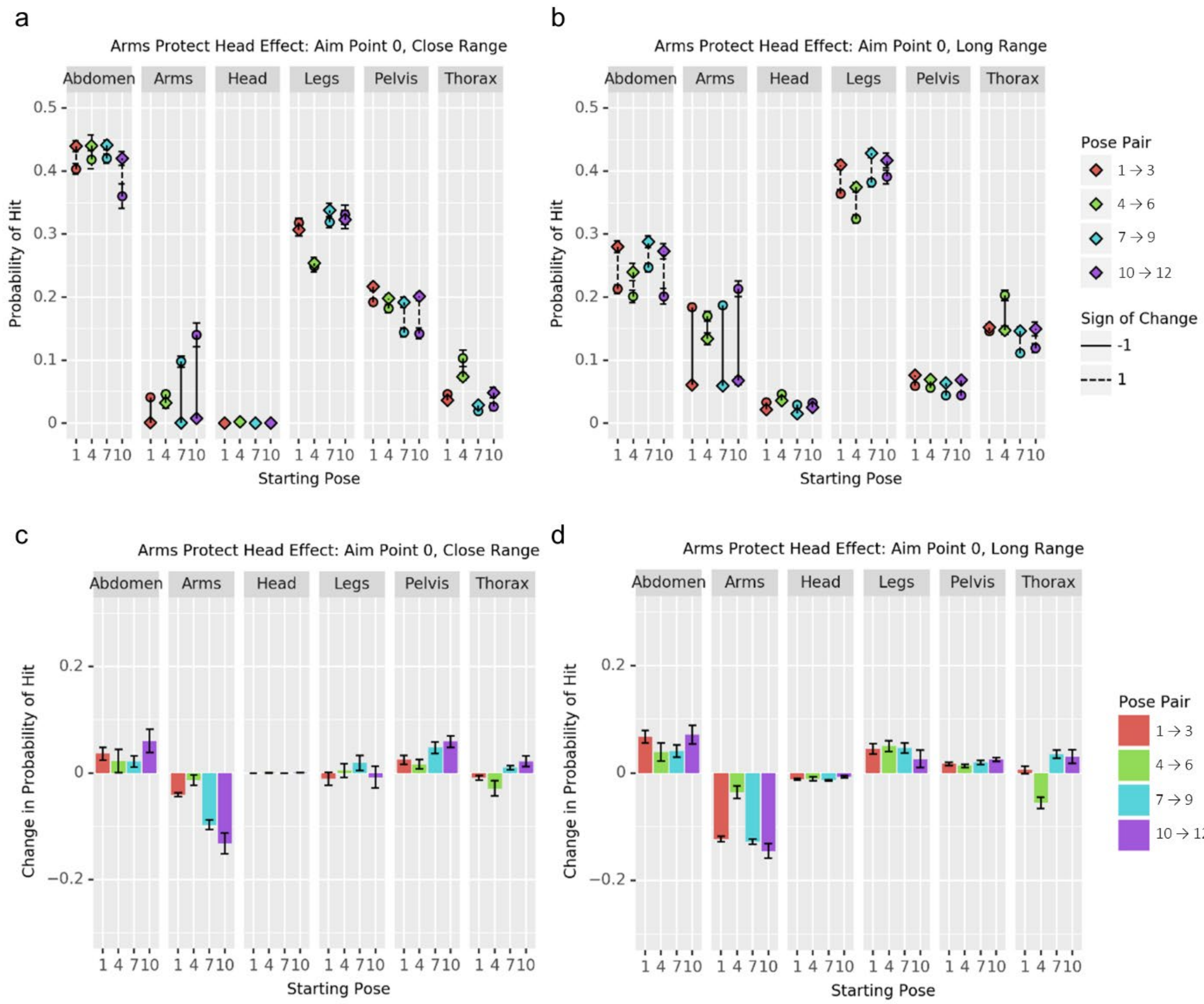

Figure C-4. Changes in Relative p(hit) Distribution Across Six Body Regions for Protect Head Action. These plots correspond to the belt-buckle aim point (Aim Point 0), with data aggregated across 52 images for each pose and body region. Color represents the starting posture in transitions defined in Table 4. (a, b) Relative *p*(hit) before (circles) and after (diamonds) the subject protects the head with the arms for (a) short-range and (b) long-range weapon dispersion. Solid lines indicate that protecting the head decreased *p*(hit) for that starting posture and body region. Dashed lines indicate that protecting the head increased *p*(hit). Error bars represent standard error of the mean for starting and ending expected *p*(hit). (c, d) Change in relative *p*(hit) for "Protect Head" posture pairs for (c) short-range and (d) long-range weapon dispersion. Error bars represent standard error of the mean for change in *p*(hit).

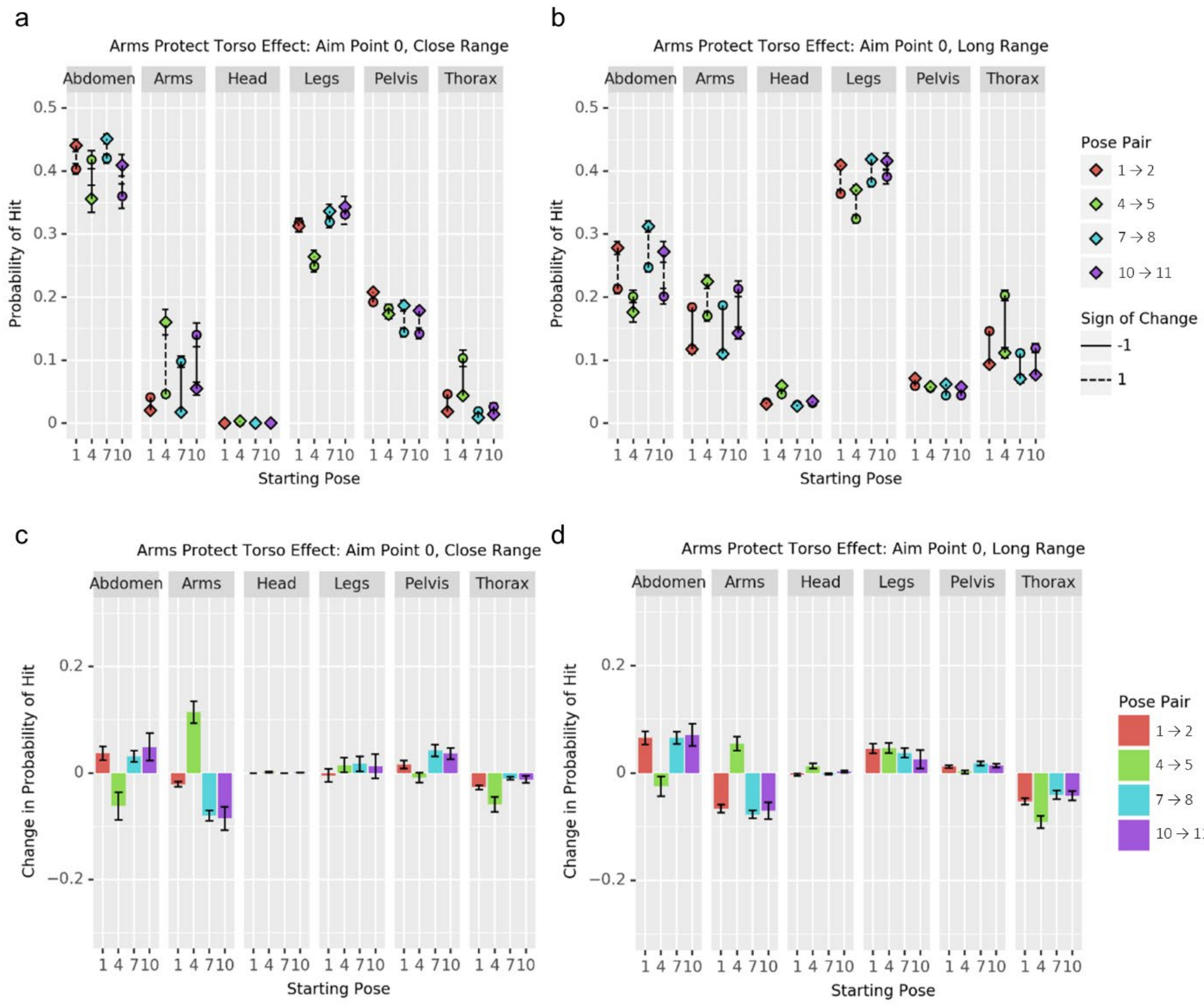

Figure C-5. Changes in Relative *p*(hit) Distribution Across Six Body Regions for Protect Torso Action. These plots correspond to the belt-buckle aim point (Aim Point 0), with data aggregated across 52 images for each pose and body region. Color represents the starting posture in transitions defined in Table 4. (a, b) Relative *p*(hit) before (circles) and after (diamonds) the subject protects the torso with the arms for (a) short-range and (b) long-range weapon dispersion. Solid lines indicate that protecting the torso decreased *p*(hit) for that starting posture and body region. Dashed lines indicate that protecting the torso increased *p*(hit). Error bars represent standard error of the mean for starting and ending expected *p*(hit). (c, d) Change in relative *p*(hit) for "Protect Torso" posture pairs for (c) short-range and (d) long-range weapon dispersion. Error bars represent standard error of the mean for change in *p*(hit).

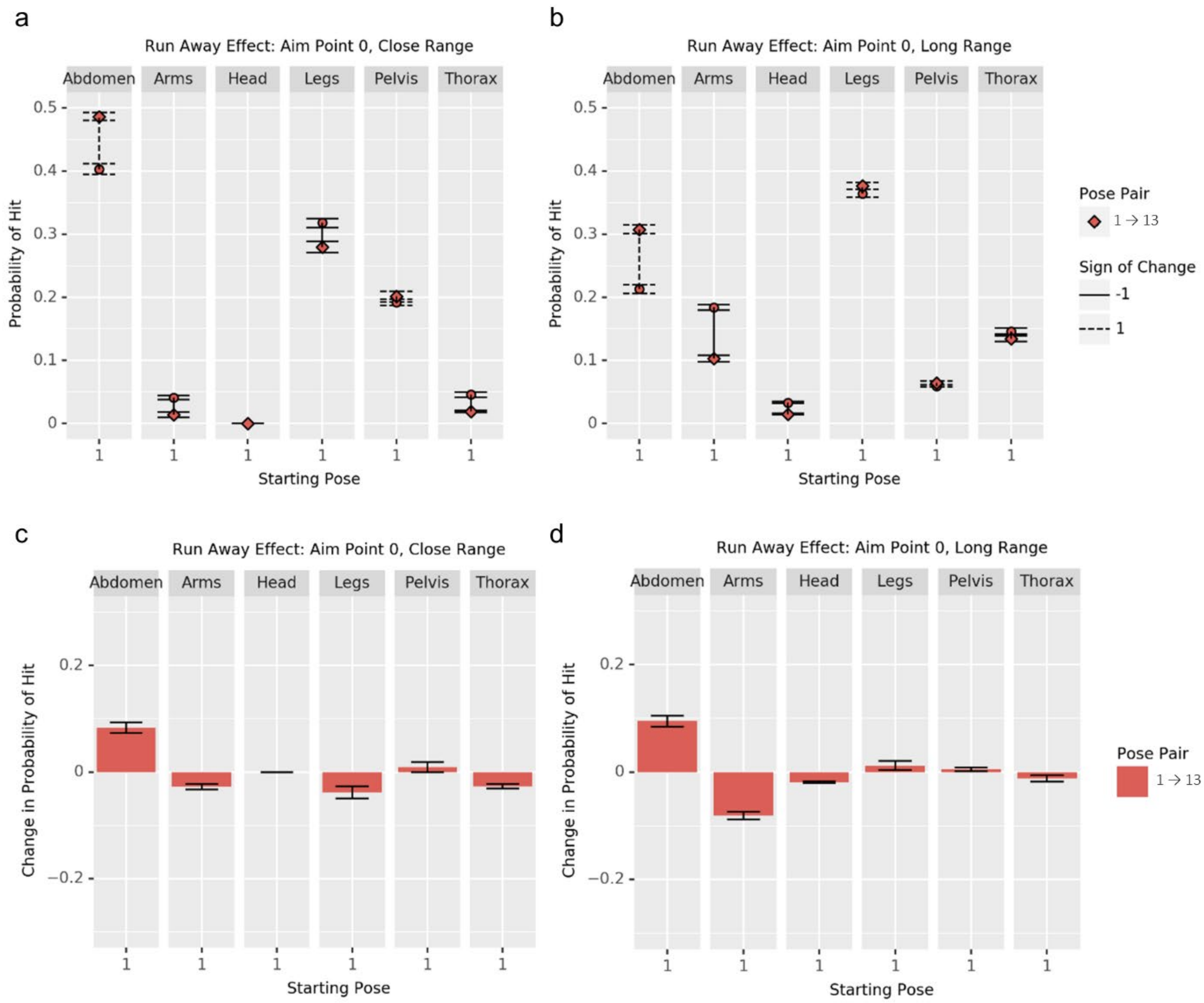

Figure C-6. Changes in Relative *p*(hit) Distribution Across Six Body Regions for Run Away Action. These plots correspond to the belt-buckle aim point (Aim Point 0), with data aggregated across 52 images for each pose and body region. (a, b) Relative *p*(hit) before (circles) and after (diamonds) the subject runs away for (a) short-range and (b) long-range weapon dispersion. Solid lines indicate that running away decreased *p*(hit) for that body region. Dashed lines indicate that running away increased *p*(hit). Error bars represent standard error of the mean for starting and ending expected *p*(hit). (c, d) Change in relative *p*(hit) for "Run Away" posture pair for (c) short-range and (d) long-range weapon dispersion. Error bars represent standard error of the mean for change in *p*(hit).

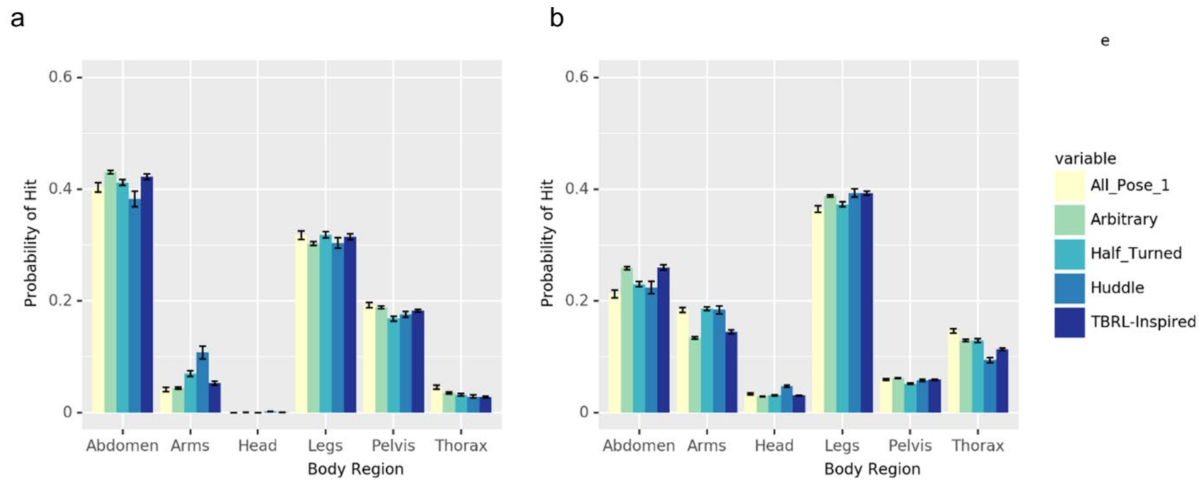

Figure C-7. Relative *P*(hit) Distributions Computed for the Belt-Buckle Aim Point at (a) Close Range and (b) Long Range for Several Example Posture Distributions. Color corresponds to posture distribution. Error bars correspond to estimated standard error of *p*(hit) for each posture distribution and body region.

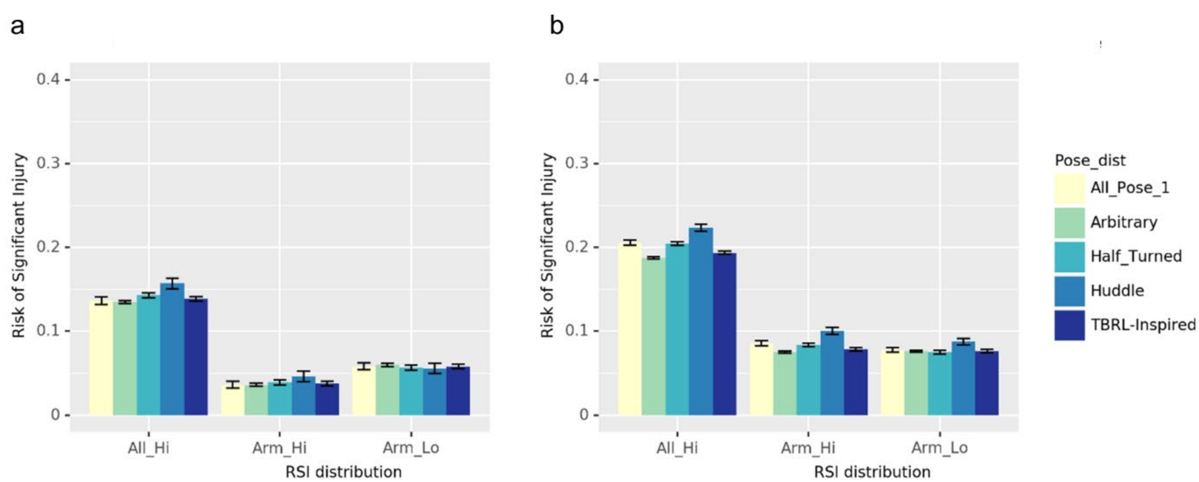

Figure C-8. Aggregate Risk of Significant Injury Computed for the Belt-Buckle Aim Point at (a) Close Range and (b) Long Range for Several Example Posture and Body-Region Specific RSI Distributions. Color corresponds to posture distribution. Error bars correspond to estimated standard error of aggregate RSI for each posture distribution and RSI distribution.

References

Chen, Lulu, Hong Wei, and James Ferryman. 2013. "A Survey of Human Motion Analysis Using Depth Imagery." *Pattern Recognition Letters* 34 (15): 1995–2006. https://doi.org/10.1016/j.patrec.2013.02.006.

DoD. 2013. "Directive 3000.03E." USD A&S. https://www.esd.whs.mil/Portals/54/Documents/DD/issuances/dodd/300003p.pdf?ver=2018-10-24-112944-467.

Hynes, Andrew, and Stephen Czarnuch. 2018. "Human Part Segmentation in Depth Images with Annotated Part Positions." *Sensors* 18.

Mahajna, Ahmad, Nabil Aboud, Ibrahim Harbaji, Afo Agbaria, Zvi Lankovsky, Moshe Michaelson, Doron Fisher, and Michael M. Krausz. 2002. "Blunt and Penetrating Injuries Caused by Rubber Bullets during the Israeli-Arab Conflict in October, 2000: A Retrospective Study." *The Lancet* 359: 1795–1800.

Mezzacappa, Elizabeth, Robert M. DeMarco, Gordon Cooke, Nasir Jaffery, Hugh Huntzinger, and Gladstone Reid. 2018. "Behaviors and Postures in Response to Threat of Blunt Impact." ARAET-TR-18xxx. U.S. Army Armament Research, Development and Engineering Center.

Olson, Kristofor A., Laura E. Haselden, R. Daniel Zaunbrecher, Adam Weinfeld, Lawrence H. Brown, Jason A. Bradley, Tatiana C. P. Cardenas, et al. 2020. "Penetrating Injuries from 'Less Lethal' Beanbag Munitions." *New England Journal of Medicine*. https://doi.org/10.1056/NEJMc2025923.

Rezende-Neto, Joao, Fabriccio D. F. Silva, Leonardo B. O. Porto, Luiz C. Teixeira, Homer Tien, and Sandro B. Rizoli. 2009. "Penetrating Injury to the Chest by an Attenuated Energy Projectile: A Case Report and Literature Review of Thoracic Injuries Caused by 'Less-Lethal' Munitions." *World Journal of Emergency Surgery* 4.

Schneider, C. A., W. S. Rasband, and K. W. Eliceiri. 2012. "NIH Image to ImageJ: 25 Years of Image Analysis." *Nature Methods* 9: 671–75.

Shen, Weixin, Eugene Niu, Charles Webber, James Huang, and Lucy Bykanova. 2012. "Advanced Total Body Model (ATBM) Analyst's Guide for Model Verification and Validation." J0939-10–389. L-3 Applied Technologies / Jaycor.

Simonds, James, Charles Webber, Eugene Niu, James Huang, Lucy Bykanova, and Weixin Shen. 2010. "XM1116 Human Effects Assessment Update." Joint Non-Lethal Weapons Human Effects Center of Excellence.

Suyama, Joe, Peter D. Panagos, Matthew D. Sztajnkrycer, Denis J. FitzGerald, and Dawn Barnes. 2003. "Injury Patterns Related to Use of Less-Lethal Weapons during a Period of Civil Unrest." *The Journal of Emergency Medicine* 25: 219–27.

Walt, Stéfan van der, Johannes L. Schönberger, Juan Nunez-Iglesias, François Boulogne, Joshua D. Warner, Neil Yager, Emmanuelle Gouillart, and Tony Yu. 2014. "Scikit-Image: Image Processing in Python." *PeerJ* 2 (June). https://doi.org/10.7717/peerj.453.

Webber, Charles, Lucy Bykanova, Eugene Niu, and James Simonds. 2012. "40 Mm HEMI Blunt Trauma Baseline Human Effects Assessment." The Joint Non-Lethal Weapons Human Effects Center of Excellence.

Abbreviations

ATBM	Advanced Total Body Model
CFR	Code of Federal Regulations
CONOPs	Concept of Operations
DoD	Department of Defense
HEMI	Human Electro-Muscular Incapacitation
IDA	Institute for Defense Analyses
IFC	Intermediate Force Capability
JIFCO	Joint Intermediate Force Capabilities Office
RSI	Risk of Significant Injury
TBRL	Target Behavioral Response Laboratory

REPORT DOCUMENTATION PAGE

Form Approved
OMB No. 0704-0188

The public reporting burden for this collection of information is estimated to average 1 hour per response, including the time for reviewing instructions, searching existing data sources, gathering and maintaining the data needed, and completing and reviewing the collection of information. Send comments regarding this burden estimate or any other aspect of this collection of information, including suggestions for reducing the burden, to Department of Defense, Washington Headquarters Services, Directorate for Information Operations and Reports (0704-0188), 1215 Jefferson Davis Highway, Suite 1204, Arlington, VA 22202-4302. Respondents should be aware that notwithstanding any other provision of law, no person shall be subject to any penalty for failing to comply with a collection of information if it does not display a currently valid OMB control number.

PLEASE DO NOT RETURN YOUR FORM TO THE ABOVE ADDRESS.

1. REPORT DATE	2. REPORT TYPE	3. DATES COVERED *(From–To)*
January 2021	FINAL	

4. TITLE AND SUBTITLE

The Role of Defensive Postures in Computing Probability of Hit for Projectile Blunt Impact Intermediate Force Capabilities

5a. CONTRACT NUMBER
HQ0034-14-D-0001

5b. GRANT NUMBER

5c. PROGRAM ELEMENT NUMBER

6. AUTHOR(S)

Bhatt, Sujeeta B.
Cheng, Emily
Kramer, Corinne M.
Swallow, Jessica G.
Teichman, Jeremy A.

5d. PROJECT NUMBER
DU-2-4273

5e. TASK NUMBER

5f. WORK UNIT NUMBER

7. PERFORMING ORGANIZATION NAME(S) AND ADDRESS(ES)

Institute for Defense Analyses
Systems and Analyses Center
4850 Mark Center Drive
Alexandria, VA 22311-1882

8. PERFORMING ORGANIZATION REPORT NUMBER

IDA Document D-21534

9. SPONSORING / MONITORING AGENCY NAME(S) AND ADDRESS(ES)

Joint Intermediate Force Capabilities Office
3097 Range Road
Quantico, VA 22134-5100

10. SPONSOR/MONITOR'S ACRONYM(S)

JIFCO

11. SPONSOR/MONITOR'S REPORT NUMBER(S)

12. DISTRIBUTION/AVAILABILITY STATEMENT

Approved for public release; distribution is unlimited (27 September 2021).

13. SUPPLEMENTARY NOTES

14. ABSTRACT

Risk of significant injury (RSI) from blunt-impact intermediate-force capabilities is computed by summing the conditional probabilities of significant injury for impacts to different body regions weighted by the probability of hit (p(hit)) for those body regions. These p(hit) distributions are typically computed without regard to the effects of target behavior. This report analyzes how p(hit) distributions are affected by defensive behaviors such as crouching, turning to the side, or moving the arms to block the head or torso. By analyzing simulated weapon-dispersion patterns overlaid on a dataset of segmented images collected for a range of defensive postures and subjects, we quantitatively evaluate the effect of defensive postures on body-region-specific p(hit) distributions for multiple aim points and weapon-dispersion patterns. We show that defensive postures cause changes in how projectile impacts from a blunt-impact weapon are distributed over the regions of the body that can affect overall RSI calculation. Note, however, that the outcome (increased or decreased RSI) is dependent not only on the set of defensive actions taken but also on which regions of the body are most vulnerable to the weapon of interest. To inform the design, training, and concept of operation of each weapon, we conclude that analysis of RSI should account for potential target responses to the intermediate-force capability.

15. SUBJECT TERMS

Intermediate force capabilities (IFCs); Joint Intermediate Force Capabilities Office (JIFCO); probability of hit (p(hit)); risk of significant injury (RSI)

16. SECURITY CLASSIFICATION OF:			17. LIMITATION OF ABSTRACT	18. NUMBER OF PAGES	19a. NAME OF RESPONSIBLE PERSON
					Burgei ,Wesley
a. REPORT	b. ABSTRACT	c. THIS PAGE			19b. TELEPHONE NUMBER *(include area code)*
Uncl.	Uncl.	Uncl.	SAR	69	(703) 432-0899

Standard Form 298 (Rev. 8-98)
Prescribed by ANSI Std. Z39.18